The dominance of large-scale phase dynamics in human cortex, from delta to gamma

David M. Alexander[1] and Laura Dugué[1,2]

1: Université Paris Cité, CNRS, Integrative Neuroscience and Cognition Center, F-75006 Paris, France

2: Institut Universitaire de France (IUF), F-75005 Paris, France

Corresponding author: david.murray.alexander@gmail.com

Abstract

The organization of the phase of electrical activity in the cortex is critical to inter-site communication, but the balance of this communication across large-scale (>8cm), macroscopic (>1cm) and mesoscopic (1cm to 1mm) ranges is an open question. Traveling waves in the cortex are spatial phase gradients, such that phase values change smoothly through the cortical sheet over time. Large-scale cortical traveling waves have been understudied compared to micro- or mesoscopic waves. The spatial frequencies (i.e., the spatial scales) of cortical waves have been characterized in the grey-matter for micro- and mesoscopic scales of cortex and show decreasing spatial power with increasing spatial frequency. This research, however, has been limited by the size of the measurement array, thus excluding large-scale traveling waves. Obversely, poor spatial resolution of extra-cranial measurements prevents incontrovertible large-scale estimates of spatial power via electroencephalogram and magnetoencephalogram. These limitations mean that the relative importance of large-scale traveling waves is unknown, and recent research has suggested waves measured extra-cranially are artefactual. We apply a novel method to estimate the spatial frequency spectrum of phase dynamics in order to quantify the uncertain large-scale range. Stereotactic electroencephalogram (sEEG) is utilized to leverage measurements of local-field potentials within the grey matter, while also taking advantage of the sometimes large extent of spatial coverage. Irregular sampling of the cortical sheet is offset by use of linear algebra techniques to empirically estimate the spatial frequency spectrum. We find the spatial power of the phase is highest at the lowest spatial frequencies (longest wavelengths), consistent with the power spectra ranges for micro- and meso-scale dynamics, but here shown up to the size of the measurement array (up to 8-16cm), i.e., approaching the entire extent of cortex. Low spatial frequencies dominate the cortical phase dynamics. This has important functional implications as it means that the phase measured for a single contact in the grey matter is more strongly a function of large-scale phase organization than local—within the same frequency band at least. This result arises across a wide range of temporal frequencies, from the delta band (1-3Hz) through to the high gamma range (60-100Hz).

Keywords: macroscopic cortex; traveling waves; phase dynamics; stereotactic EEG; intra-cranial.

Introduction

Traveling waves (TWs) have been described in human cortex since at least 1949 (1). They are a commonly described class of the more general phenomena of cortical phase dynamics, which we define as the set of all possible phase patterns. TWs may take the form of linear gradients (2–5), phase cones (6,7), spirals (8–10), and may also vary in velocity, i.e., ranging between standing and pure traveling waves (11,12). Large-scale TWs, specifically, are monotonic phase gradients measured over more than 8cm, up to the global scale of the cortical sheet.

Theoretical analyses have long predicted the existence of macroscopic wave dynamics (13–15). Technically, the measured waves are group waves in the physical sense (16), that is, we measure the envelope of the heterogeneous activity at some temporal frequency (TF) as it moves through the cortex. The waves observed in neural mass models arise through a dynamic balance of excitation and inhibition and activated fields radiate outward from previously activated areas (13,14,17–19). Mathematical analyses indicate activity modes that are associated with damped TWs (14), and under appropriate boundary conditions, these correspond to large-scale TWs (see **Figure 1**). These waves are best understood as being coordinated by long-range myelinated axons (17). Being group waves, they do not directly indicate the velocity of information transmission (13,20), that is, the speed of transmission of axonal volleys (c.f. 18,19). They do, on the other hand, reflect the speed at which regions of activity can flip between different regimes, often as the result of small changes in coordinated synaptic inputs (20, c.f. 21).

Alternative hypotheses have been proposed to explain large-scale TWs measured extra-cranially. We highlight three prior studies (21,22,25) here due their clear and explicit mathematical treatments, enabling an effective collision with the present research. Local TWs, driven by short-range intracortical connectivity, have been proposed as the origin of the extra-cranial measurements (21,22), as shown in **Figure 1**. Since these waves move slowly in the grey matter, but over a local region, when projected to the scalp they reproduce the fast velocity characteristics of the reported extra-cranial alpha waves (26–28). Another explanation for macroscopic TWs is in terms of localized oscillating cortical sources mixing at the sensor level (e.g., in electroencephalography, EEG). In this approach, two spatially offset and phase-lagged components are derived experimentally by source modelling, which in turn reproduces the measured extra-cranial waves (20,24; see **Figure 1**). Importantly for the present research, the dynamics associated with the alternative hypotheses can be re-represented as Fourier spectra of grey-matter activity, and these spectra give distinct and measurable predictions.

For the veridical TWs hypothesis, the expected peak in the spatial frequency spectrum of phase is at a low spatial frequency, while the alternative hypotheses for artefactual large-scale TWs predict peaks at higher spatial frequencies (SFs). In order to test these hypotheses, we therefore estimate the relative power of different bands of SFs comparing high (SF>16 cycles/m) to low (8<SF<16 cycles/m) SF contributions to the measurable phase; these SFs are approximately equivalent to wavelengths ($\lambda = 1 / \mathrm{SF}$) of λ<6cm vs. 6<λ<12 cm.

The alternative explanations that have been proposed for measurements of extra-cranial macroscopic TWs rely on two assumptions. First, for the localized activity to meaningfully reproduce the sensor level measurements, the activity proposed must dominate during the event; that is, the local TWs or oscillatory sources must arise within a relatively quiescent

cortex. Otherwise, the local waves or oscillatory sources, as measured extra-cranially, will be washed out by the cortical activity that actually dominates. The second, and related assumption, is that measures aggregated over samples and/or trials accurately reflect relevant signals in single sample data (29). This aggregation assumption is related to the quiescence assumption because it allows local waves or oscillatory sources to be detected in otherwise 'noisy' environments. Typical sample aggregation procedures, such as averaging in event-related potentials, reverse correlation or computing the lead-field matrix in source localization, result in activity with high variation across aggregated quantities being made quiescent, thereby treating this activity as noise (29). By contrast, the present study estimates SF via low dimensional representations of the phase matrices using singular value decomposition (SVD), rather than for sample aggregates (e.g., trial means). SVD is a lossless decomposition of a participant's phase data, up to the choice of cut-off rank for exclusion of noise-like phase vectors.

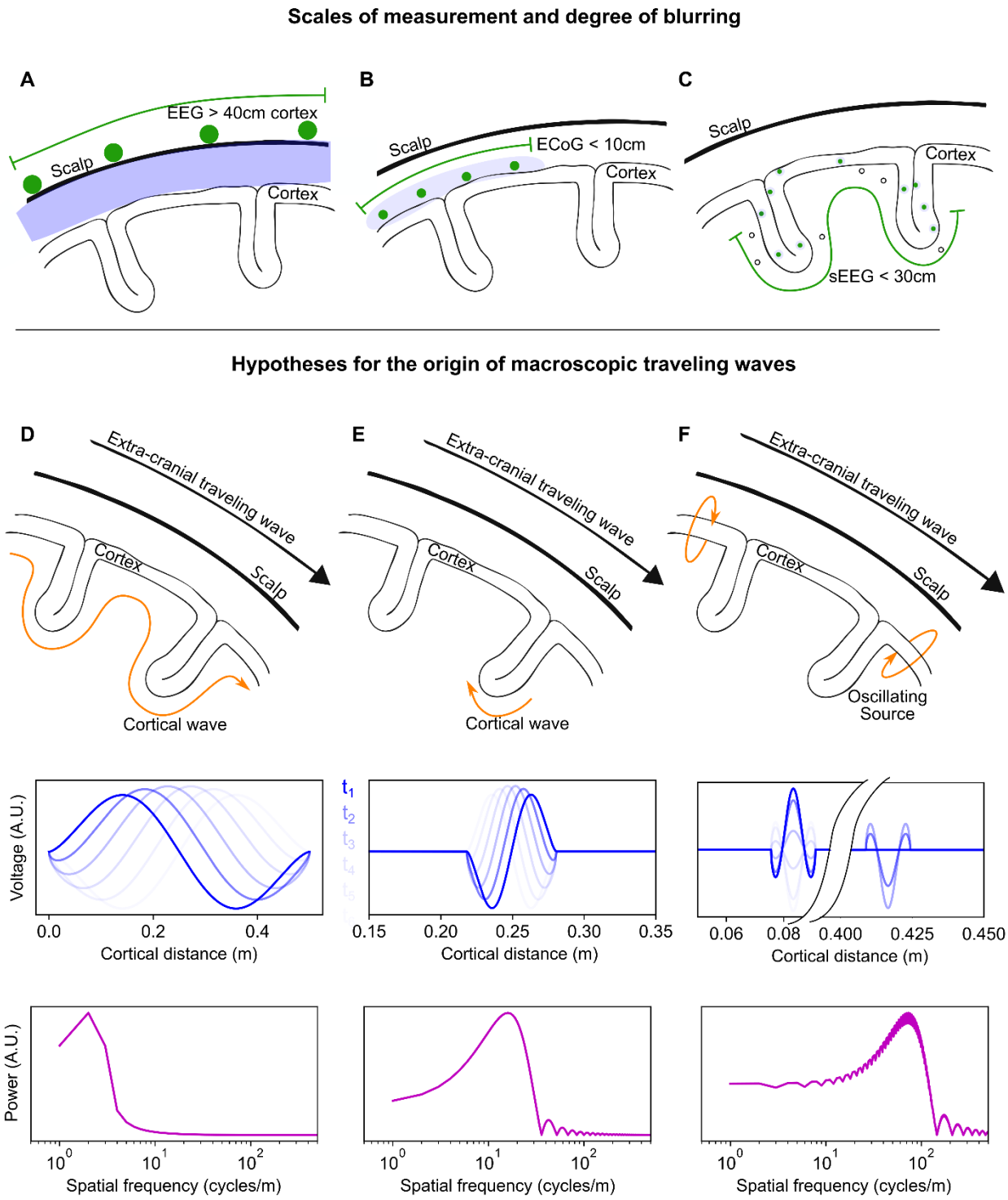

Figure 1*. Traveling waves, measurements and origin.* ***A-C****. Scales of measurement and degree of blurring in EEG, ECoG and stereotactic EEG. The maximum linear distances of unfolded cortex typically covered by each technique are shown in each panel.* ***A****. EEG measures the electrical activity of the cortex at the surface of the scalp (contacts shown in green). Due to volume conduction in the intervening tissues (blue), the cortical signal is highly blurred and preferentially samples gyri. The EEG array covers the entirety of the scalp in a quasi-regular grid, enabling a large extent of cortical coverage (green line, not to scale).* ***B****. Electrocorticogram (ECoG) measures the electrical activity of the cortex at the cortical surface. The volume conduction effects are less here, but the measurement array preferentially samples activity at the gyri. The distance between contacts is regular, forming a two-*

dimensional measurement array, but the size of the array is limited to 10cm or less. ***C****. Stereotactic EEG measures electrical activity within the grey matter of the cortex, and therefore has a lower degree of blurring. The clinical placement of the linear arrays of contacts result in a highly irregular measurement array, though often with wide coverage of the cortex, though in general less than 30cm.* ***D-F****. Hypotheses for the origin of macroscopic TWs measured extra-cranially (adapted from 14).* ***D****. Extra-cranial TWs reflect real, coordinated, spatio-temporal activity across the entire cortex. The TWs are measurable at the scalp because the dominant spatial frequency of the activity has a long wavelength and is therefore detectable at the scalp. A sinusoidal wave corresponding to this hypothesis is shown in blue, with successive time samples in lighter shades. The fast Fourier transform of the model wave is shown in magenta. The expected spatial frequency spectrum, when measured in the grey-matter, has a peak at a low spatial frequency.* ***E****. A local wave (shown here in a sulcus) slowly traverses a small region of grey matter via intracortical connections. The wave appears at the scalp as a fast-moving global wave due to volume conduction effects. The wave's (blue) expected spatial frequency spectrum (magenta), when measured in the grey-matter, has a peak at a high spatial frequency.* ***F****. Localized oscillatory sources that are out of phase appear as large-scale TWs at the scalp due to volume conduction effects. The oscillators' (blue) expected spatial frequency spectrum (magenta), when measured in the grey-matter, has a peak at high spatial frequencies corresponding to the size of each oscillatory source, with a weaker elevation in low spatial frequency power due to the interaction between sources.*

Previous research has consistently revealed that the spatial power of phase decreases monotonically with SF. Intracranial measurements show that the SF spectrum of phase declines with power from 12 cycles/m (8cm wavelengths) (2,7,8,29–31). The estimates, however, use cortical surface arrays with limited spatial coverage (≤8cm) and were therefore insensitive to longer wavelengths (see **Figure 1**). Likewise, animal studies also point to a SF spectrum for phase that monotonically decreases in power with increasing SF (6), but at measurement scales of 7mm or smaller (6,32–34). Estimates of the relative contribution of large-scale TWs to the SF spectrum of cortical phase dynamics have used EEG (7,30) (see **Figure 1**) or magnetoencephalogram (MEG) (11), and consistently describe a SF spectrum with maximum power at wavelengths near the array size, and decreasing in power with smaller wavelengths.

These studies, collectively, have not been able to unambiguously determine the relative importance of low SF components. Fourier analysis is sensitive to the sampling of the underlying data, both at the smallest range (the sampling frequency) and the maximum range (the size of the array) (35). Phase dynamics at the largest cortical scales, as broad-band signals, cannot be assessed using small intra-cortical arrays. Obversely, extra-cranial measurements are contaminated by volume conduction artefacts (EEG) or blurring by distance to the sensor array (MEG), both of which act as a low pass filter (18,29,36) (see **Figure 1**). A low pass filter will suppress higher SFs, thereby inflating the relative effect of the low SFs quantified from the phase dynamics and introducing an ambiguity. In the present research we use cortical depth electrodes to assess that part of the SF spectrum of phase between 8 and 50 cycles/m. Stereotactic EEG (sEEG) contacts have excellent spatial resolution and coverage (although sparse and irregular) which can extend to 25cm of the cortical sheet. By extending grey-matter measurements of the SF spectrum to longer wavelengths, we were able to accurately assess the relative contribution of large-scale phase dynamics to cortical activity.

The numerical methods described in the present research are novel. The spatial pattern of contacts in sEEG within the cortical grey matter has a high degree of irregularity and sparseness. In addition, the contacts are embedded in a thin, three-dimensional sheet. Viewed globally, the sheet covers the surface of a highly convoluted, three-dimensional, distorted spheroid. While methods exist for Fourier analysis on irregular grids (37–41), the combination of irregularity, sparseness and distortion in sEEG makes them unsuitable for the present research question. Methods also exist for computing spatial derivatives on irregular grids, but these generally assume denser sampling within a continuous volume (42). In the present research, we use a multi-scale, finite difference method to compute the SF of the phase, which is first estimated at each TF. To avoid spurious phase estimates, we first decompose the phase vectors into patterns of spatial covariance using SVD, retaining only spatial components that explain non-trivial amounts of variance.

In the present research we estimate the SF of the cortical *phase* dynamics. This means removing the amplitude information from the initial Fourier components estimated at each temporal frequency. This removal is for two reasons: (1) consistency with the research on TWs and other phase dynamics and (2) the assumption that the absolute amplitude measurable at each contact is a source of noise, since it depends on the exact details of contact placement which are not as exact as experimental studies in animals.

Despite the published research on SF spectra of cortical phase dynamics (6,7,30,43), decades of neuroscience research has favoured explanations of extra-cranial measurements in terms of mesoscopic TWs or focal cortical sources mixing at the sensor level (21,22,25). Here, we can provide a concrete test of the alternative hypotheses based on a simple criterion. We remove ambiguities in the measurement of purported macroscopic TWs by quantifying them within the grey matter. Consequently, the proposed mechanisms of localized TWs, oscillating sources or large-scale phase gradients can be tested against the SF spectrum of phase measurements for consistency with the proposed mechanism, as shown in **Figure 1**. Specifically, the characteristically small spatial scale of the proposed mesoscopic waves or oscillating sources will be revealed as maxima (or local maxima) in the SF spectrum. These high SF components have been hypothesized to combine, via blurring of signal, to form apparent low SF macroscopic TWs at the sensor level (21,22,25). This effect will therefore only be apparent if other cortical activity is relatively quiescent; the high SF components must really be a prominent part of the signal. Alternatively, a finding that low SF components dominate the spectrum of phase, at distances corresponding to large-scale TWs, cannot support the blurring or source mixing explanation for macroscopic TWs. This is because the sensor level measurements will in turn be dominated by the real low SF component of the cortical phase dynamics. Measurement of macroscopic TWs in EEG or MEG can only create a purely artefactual low SF gradient of phase, through mixing and blurring, if no such gradient dominates the underlying signal in the first place (compare **Figure 1A & 1D**).

Results

Overview

In the present research we analyze a publicly available data-set (RAM Public Data https://memory.psych.upenn.edu/RAM_Public_Data). We report the results from 23 participants. Note that most subsequent procedures (construction of spatial frequency spectra, statistical testing of link to measurement array size and TF) were carried out at the single participant level, so each participant comprises a test of the hypothesis under scrutiny. The sEEG contacts in the grey matter were re-referenced using the pooled average of the 50% lowest signal amplitude white matter contacts (44). A typical participant's contacts are shown in **Figure 2A**. From the sEEG time-series, complex-valued phase was analyzed at 34 frequencies, using short time-series methods (2 cycle Morlet wavelets). Centre frequencies ranged from 1.0 to 97.0Hz, on a logarithmic scale. A segment of typical phase data with a centre frequency of 9.2Hz is shown in **Figure 2B**.

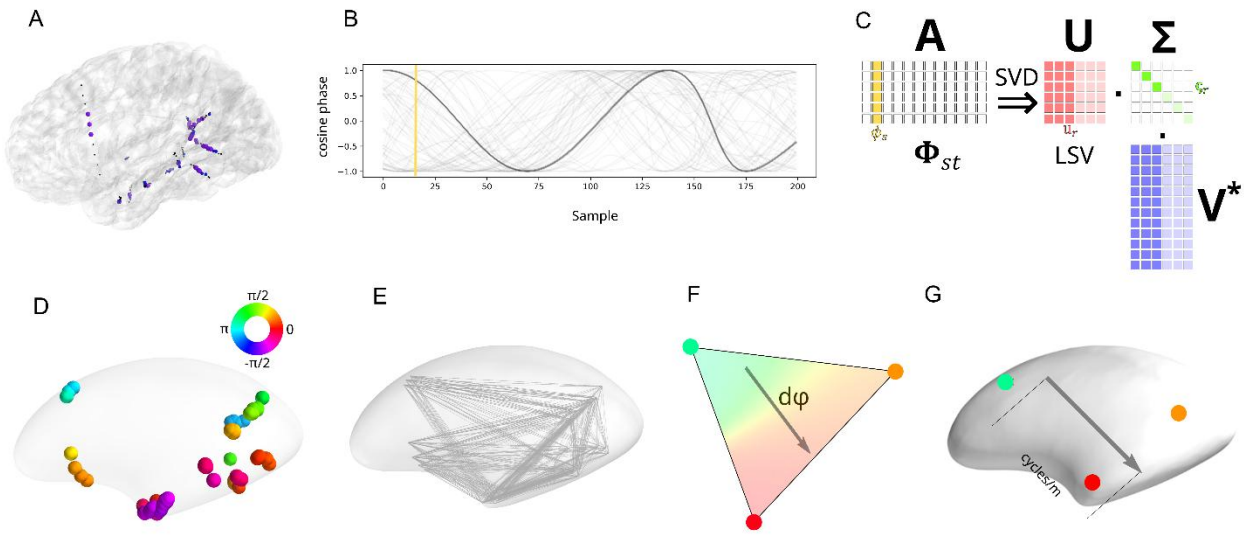

Figure 2. *Schematic of data processing pipeline.* ***A****. Cortical reconstruction of one participant, showing placement of sEEG contacts. Grey matter contacts are shown as black dots. White matter contacts are shown with colored circles (blue, or purple for contacts with 50% lowest amplitude signal).* ***B****. The phase values of a segment of data at filtered at 9.2Hz (real part only) is shown for all grey matter contacts in one participant. One contact's phase values are shown in darker grey. A single vector of phase is indicated with the yellow line.* ***C****. SVD decomposes any matrix,* **A***, into three separate matrices consisting of a rotation (***U****, the LSVs), a scaling (***Σ****) and another rotation (***V****, the right singular vectors). Here, the matrix of complex-valued phases for a participant at some centre frequency,* $\mathbf{\Phi}_{st}$*, is decomposed into LSVs that represent typical patterns of phase (red vertical bars). The values along the diagonal of* **Σ** *give the overall weighting of each LSV in the original matrix. The right singular vectors give the changing time-course for each of the LSVs in the original matrix (blue vertical lines). The bright and pale reds, greens and blues indicate how the least important components (pale) may be dropped, combining a small number of most important components to form a good approximation of the original matrix.* ***D****. Placement of grey matter contacts within inflated left hemisphere of cortex. Phase angles of a LSV indicated on the rainbow scale. Phase angles are shown on the colour wheel.* ***E****. Flattened representation of the approximate equilateral triangles of grey-matter contacts, into which the LSV values are resampled as triplets of values.* ***F****. Triplets of values from each LSV were used to estimate the rate of change of phase over regions of the cortex. The direction of phase change is indicated with grey arrow, and phases have been interpolated*

between vertices of the triangle for visualization purposes. ***G****. The rate of phase of change of a triangle of contacts is converted to estimated spatial frequency over that region by incorporating the geodesic distances into the numerator. The inflated cortex is shown here, but the geodesic distances are calculated from the folded cortex i.e. shown in* ***A****.*

The highly irregular sampling grid provided by the sEEG limits the statements that can be made about the cortical phase dynamics. Due to the inherent noise of the spatial array, it was not possible to assess the smoothness of the cortical phase dynamics in the present research. We therefore consistently refer to the SF of the cortical phase dynamics and separately discuss implications for TWs. Assessment of the ubiquity of smooth gradients of phase, TWs, has been made elsewhere (11,29).

The present research used linear algebra techniques to empirically construct a basis with which to decompose the phase signal, following and extending previous techniques (4,8,11). From this simpler set of empirical functions (45) we are able to estimate the spatial frequency spectra of the cortical phase dynamics. The general strategy for empirical construction of a basis using SVD is illustrated in **Figure 2**. In the present research, the phase data at each TF was entered into an SVD. The left singular vectors (LSVs) from the SVD comprise maps of spatial covariances in phase. There are important mathematical relations between SVD and Fourier analysis and for appropriate signals (see **Methods**) the SVD will empirically recover approximate sinusoidal basis functions.

In **Figure 3**, we present examples of the use of SVD to decompose signals into components approximating the Fourier basis. **Figure 3A** shows a one-dimensional random walk. Figure 3B shows how SVD decomposes this signal into pairs of sinusoids of increasing TF. These sinusoid pairs are quantitatively similar to the family of one-cycle Morlet wavelets (see 45 for a mathematical proof). **Figure 3c** shows an image of waves of water. We encoded the image as 'time-series' of phase at the dominant vertical frequency, then analysed the 'spatial' vectors of phase in the horizontal dimension using SVD. The LSVs are approximate sinusoids corresponding to the Fourier series in the spatial dimension. **Figure 4A** shows how the corresponding singular values of these LSVs (as amount of variance explained) can be read as a power spectrum, with each successively higher SF component explaining less of the variance in the phase encoded image. **Figure 3F** shows how these methods have been applied to MEG data (4,11,29) to extract global TW components of the signal, and components at higher SFs. Here, successive groups of LSVs from the MEG phase data show increasing wavenumber (approximately k=1, k=2 …). **Figure 4B** shows the SF spectrum computed for each of these *wave maps* using the method presented in the current research. The sum of these separate spectra represents the SF spectrum for the phase at this TF in the MEG.

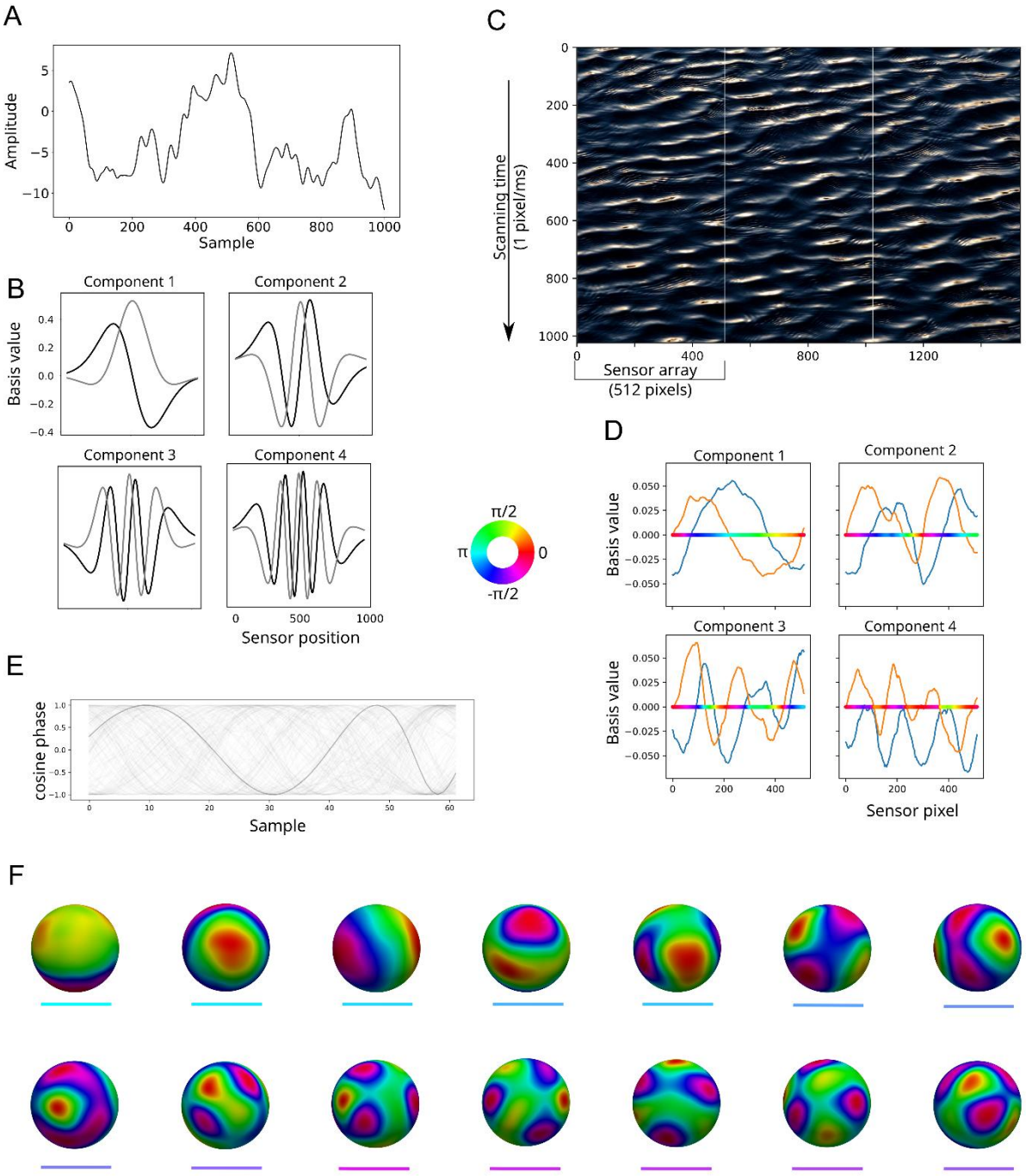

Figure 3. *Relation between SVD and Fourier analysis.* ***A****. A random walk of t time-steps is first filtered to remove very low frequency components, then successive segments (w=1024 samples) from the time-series are windowed with a Gaussian to produce a Hankel matrix* $\mathbf{A}_{wT}$*, where T = t - w/2. Here, the one unwindowed sequence of the filtered random walk is shown.* ***B****. The LSVs of the matrix* $\mathbf{A}_{wT}$ *come in pairs, with each pair approximating the real and imaginary parts of a one cycle Morlet wavelet. Here, the first four such pairs are shown, showing increasing frequency of the empirically derived Fourier components. The frequency of the first pair is closely tied to the size of the windowed sampling array.* ***C****. Image of waves. The waves have a peak spatial frequency at 15 cycles per 1000 pixels vertically, and this dimension is treated as if it were time by scanning down the image (nominally) at 1ms per pixel. The waves in the image are aligned diagonally, moving towards the bottom right. The waves complete approximately one cycle every 512 pixels in the horizontal direction. This is the width chosen for the size of the measurement array, scanning the image vertically three*

times (white boundaries). The complex-valued phase at 15Hz along the 'temporal' (vertical) axis is first calculated, and the phase dynamics along 'spatial' (horizontal) dimension are extracted using SVD. ***D****. First four components of the SVD of the vector of phases from image in* ***C****. Real part of the component is shown in blue, imaginary part in orange. The phase angle corresponding to these real and imaginary values is shown by the coloured horizontal line, with phase values shown on the colour wheel. The first plot shows the dominant 'spatial' (horizontal) frequency, captured as a single cycle wave. Each successive component has an increment in number of cycles represented, from the previous.* ***E****. Time-series of (the real part of) phase extracted from MEG data recorded with 151 magnetometers, here filtered at a centre TF of 9.2Hz. One sensor's data is highlighted in darker grey.* ***F****. Wave maps* (4) *extracted from the participant's phase data at 9.2Hz. The MEG sensors are mapped to a sphere, and phase values interpolated (values indicated by the colour wheel). The head is viewed from the top, with the nose pointing left. The first three maps show global patterns of phase, with directions of flow characteristic of MEG data, namely left-right, inferior-superior and anterior-posterior* (4,29)*. These global patterns of phase are used to extract the dominant SF of TWs in the data* (8,11)*. The components in this type of analysis are inherently spatio-temporal, since a spatial vector of smoothly changing phase implies a traveling wave over time. Successive groups of LSVs indicate components of the signal with increasing SF. (coloured lines below each map correspond to the spectra lines in* ***Figure 4B****)*

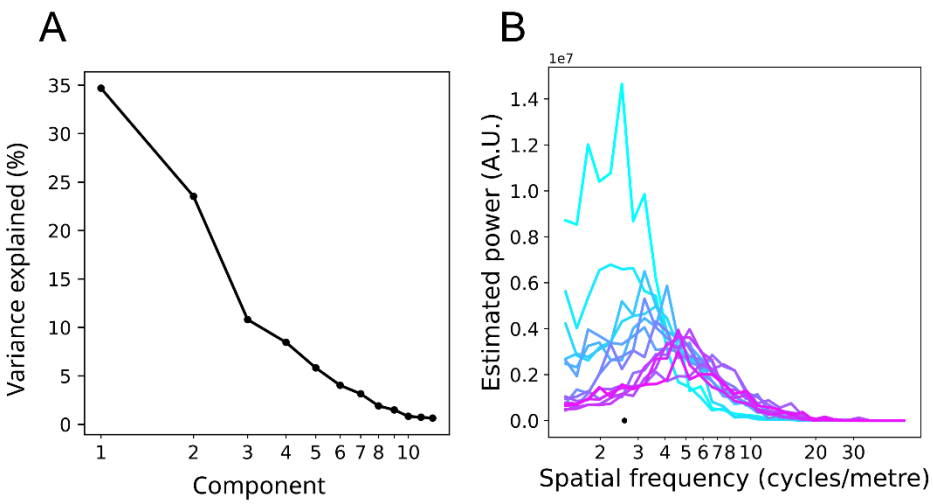

Figure 4. *SVD and estimating spectral power.* ***A****. Singular values obtained from SVD of the phase vectors from the image shown in* ***Figure 3C****. Because the first four components from the SVD are approximate sinusoids, the Fourier spectrum can simply be estimated by reading off the singular values (shown here as % variance explained). The dominant spatial frequency is at wavenumber equals one cycle per 512 pixels (the size of the array), and the next highest SF components contribute successively less to the signal.* ***B****. Estimated phase spectra for the wave maps of MEG data shown in* ***Figure 3F****, computed by the present method. The line colours correspond to the line labels in* ***Figure 3F****, the black dot indicates the SF equivalent to the maximum distance between sensors. The spectra peak at a range of different SFs, with the global maps in* ***Figure 3F*** *showing the lowest SFs and highest power, and maps 6-14 showing the highest SF and least power.*

The irregular sampling of cortical spatial coordinates in the sEEG poses a difficult problem for standard Fourier analysis, even for specialized techniques targeting non-uniform arrays (37–39,42). Here, we make use of SVD to empirically decompose the phase data, before using multi-scale differencing on each LSV to compute the SF spectrum. The primary reasons for using SVD were (1) to prioritize patterns of high spatial covariance and so exclude noisy phase estimates, and (2) an assumption that the LSV vectors represent Fourier-like components of the signal, being a combination of the smooth sinusoidal bases recoverable from regular measurement arrays (45; and **Figure 3**) and low rank corrections to 'noisy' spatial sampling (40; see **Methods**). This assumption is supported via surrogate testing of our method using brain signals whose SFs is known (i.e. MEG).

The irregular sampling of cortical spatial coordinates inherent in sEEG was overcome by first decomposing the phase matrix (columns of contacts by rows of samples, at a given TF) into components that capture the largest portions of spatial covariance in the phase signal. The LSVs of the SVD (**Figure 2C**) were then further quantified using multi-scale finite difference methods to estimate the spatial frequency spectrum. The multi-scale difference methods consisted, first, of reorganizing the sEEG contacts into triplets corresponding to the vertices of approximately equilateral triangles within the cortical sheet. Between-contact distances were calculated as geodesic distances (47) in the cortical sheet to accurately reflect the underlying topology of the cortex. See **Figure 5** and **Supplementary Figure 1** for examples of geodesic paths on the cortical surface. These triangular areas were used to calculate the rate of phase change across each region of the LSV of phase. These techniques enabled the spatial frequency spectra of the cortical phase dynamics to be quantified for cortical regions of varying area, and this was done at each TF.

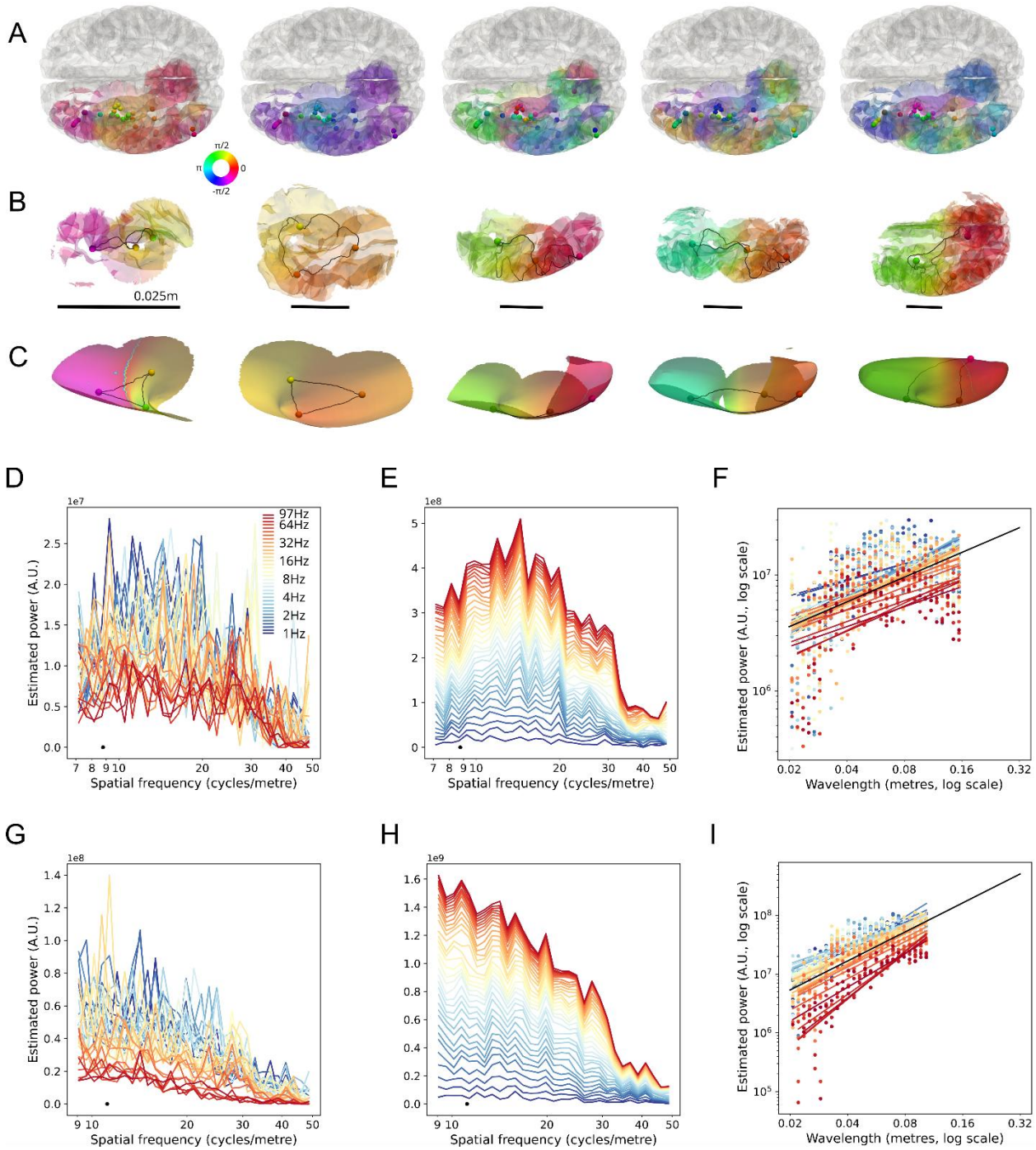

Figure 5. *LSVs of sEEG participants, equilateral triangles of LSV phase and estimated SF spectra for two partcipants.* ***A****. Cortical surface with phase values of the first five LSVs from a single participant at centre TF 3.5Hz. Grey-matter contact locations are shown with spheres, and the phase value of the LSV at each site is shown on colour scale. Phase values on the cortical surface are interpolated between contacts for visualization purposes.* ***B****. Examples of approximately equilateral triangles of contacts, used to calculate the SF spectrum. The shortest geodesic distance between contacts is shown with the black line. Phase on the section of cortical surface is interpolated for visualization purposes. The scale of each equilateral triangle (square-root of triangle area) is indicated with the black reference bar.* ***C****. Same examples shown in* ***B****, except projected onto the inflated cortex to show the unfolded triangle.* ***D****. SF spectra for one participant, over TFs 1.0 to 97.0Hz (colour scale). The largest triangle size is indicated with the black dot.* ***E****. Same as* ***D****, except shown as a stacked spectrum.* ***F****. Regression lines for (logarithm of) wavelength versus SF power at all temporal*

*frequencies (coloured lines), for the participant shown in **D** (only regression lines significant at p<0.05 shown). Spectrum values shown with coloured dots. The mean regression line (mean of slopes and offsets of significant regressions) is shown with a black line and extended to 0.32m wavelength for visualization purposes. **G**. SF spectra for a second participant. **H**. Same as **G**, except shown as a stacked spectrum. **I**. Regression lines for wavelength versus SF power (coloured lines), for the participant shown in **G**. Conventions the same as **F**.*

Single participant tests

We first quantified the estimated spatial frequency spectrum for all single participants, across all temporal frequencies. Two participants' results are shown in **Figure 5**. Lower temporal frequencies had more SF power than higher temporal frequencies (permutation test, $p<0.05$; **Panel A, D**). However, this is in large part to the better signal-to-noise ratio in the estimation of phase for the former (more time-samples in the 2-cycle Morlet wavelet) and similarly better signal-to-noise in signal measurement (higher signal amplitudes at low TFs). The effect is not necessarily a feature of higher TF signal *per se*. **Panels B & E** show the same spectra stacked over TF, and reveal the characteristic shape of the estimated spatial frequency spectrum. The spectra peak in power at a wavelength approximately equivalent to the size of the largest equilateral triangle defined on the measurement array, sometimes at a slightly lower SF. The spatial power of the phase dynamics decreased monotonically with increasing spatial frequency (permutation test over temporal frequencies, $p<0.05$). Within the range beginning at the maximum triangle size in the measurement array (equivalent to ~8.5 and 11 cycles/m in these cases), the spatial power drops steeply, before flattening at higher spatial frequencies.

This effect was statistically significant in 19 out of 23 participants (permutation test over temporal frequencies, $p<0.05$; see **Supplementary Figures 2** and **3**). All participant's mean SF slopes trended in the same direction, with participants in the top 50%, by numbers of triangles, all being significant at $p<0.001$. This suggests a practical cut-off value for number of triangles in the present method of n=1500 for being able to construct sufficiently low noise spectra to indicate a significant trend of SF versus SF power. This equates to around 50 grey-matter contacts. Only one of 782 distinct participant × TF regressions was significant with a slope in the opposite direction. We therefore conclude that SF of phase had the highest power at the lowest SF. This main result is consistent with previous studies of spatial frequency of cortical phase dynamics: the spatial power decreases with increasing spatial frequency (6,7,30,43). The present results extend the previously measured spectrum into scales equivalent to a large fraction of the cortical size.

Examples of the low SF phase dynamics are shown in **Supplementary Videos 1**, **2** and **3**.

Surrogate tests

We used surrogate methods to perturb the sEEG phase signals with artificial signals whose ground truth SF was known. This perturbation was done over a wide range of relative weightings between real and surrogate signals. If the method accurately measures SF, addition of the surrogate signals will induce a peak at the SF of the surrogate signal, increasing in relative amplitude as the surrogate signal amplitude is increased. Examples of the surrogate signal are shown in **Supplementary Figure 4. Figure 6A** shows the results for one participant at 9.2Hz, perturbed by a surrogate anterior-posterior gradient at three different SFs. The shift in the peak of the SF spectrum is apparent at low levels of injection (1/3 ratio) of the surrogate signal, consistently toward the SF peak of the surrogate. As the perturbation increases in

weight, the surrogate contribution to the spectrum becomes clearer. The perturbation is approximately at the correct SF when twice the strength of the empirical signal (2/3 ratio) and remains so until ratio 7/8.

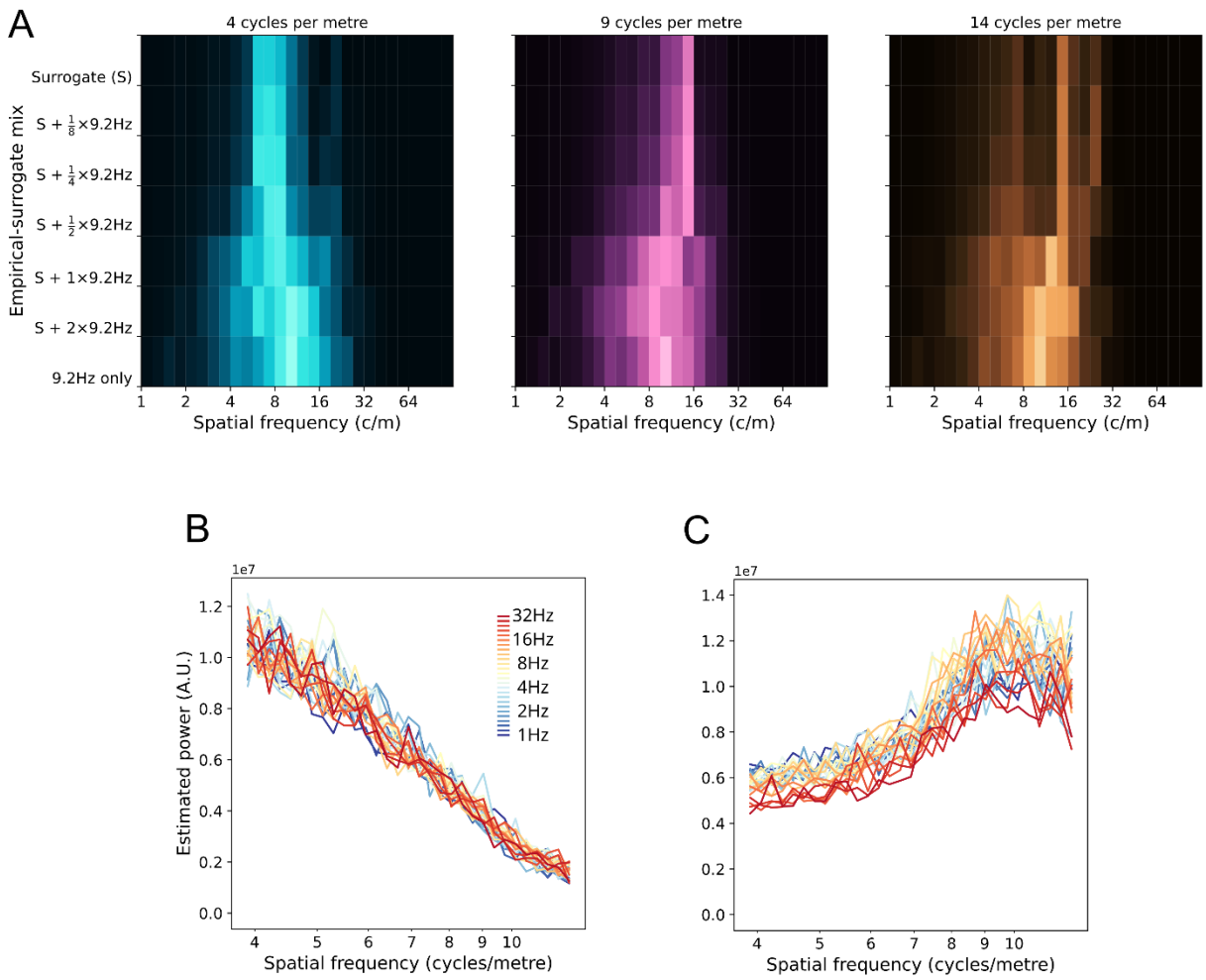

Figure 6. *Surrogate tests on individual participants.* ***A****. Effects of injection of veridical SF surrogate signal on the empirically derived spectrum. Left panel shows the spectrum of a pure surrogate signal (S) with an anterior-posterior gradient and a SF at 4c/m (top row). The empirical spectrum for phase of this participant at a centre frequency of 9.2Hz is also shown (bottom row). The effects of different weightings of empirical and surrogate signal vary vertically over the plot. Middle panel follows the same conventions, except a surrogate signal at 9c/m is shown. Right panel shows the effect of a surrogate signal at 14c/m.* ***B****. SF spectra of phase for a participant with MEG measurements. Each spectrum shows the characteristic monotonic decrease in power with increasing SF. This data is from the same participant as* ***Figure 4B****, where the unsummed spectra for each LSV at 9.2Hz are shown.* ***C****. SF spectra for surrogate MEG measurements. Here, the singular values of the first 28 components are reversed in order before reconstructing the phase time-series, creating phase signal in which high SFs dominate. The plot shows that the present methods successfully characterize the surrogate signal as SF spectra with slope reversed from the empirical signal.*

The surrogate SF signals were tested over 14 steps for a wide SF range (2c/m to 16c/m) and showed the same correct linear relation at each TF of empirical component of the phase. This was tested by regression of SF peak versus SF of surrogate (repeated for each surrogate

direction and surrogate weighting) and was significant down to and including the 1/2 surrogate ratio (permutation tests over participants, $p<0.001$, ratio 1/3 not significant). Another example of surrogate tests on the same participant is shown in **Supplementary Figure 4**, here with a left-right gradient imposed over the same set of SFs. The Figure also shows cross-participant averages for these surrogate runs. Also shown are SF spectra with pure surrogate signal, giving a clear idea of the residual noise levels in the SF spectra estimation, since the only source of noise in this case is the irregularity of the sEEG array. Due to the highly irregular sampling of the cortex, the exact locations of the peaks for the veridical SF surrogate varied slightly from participant to participant for the same surrogate SF, but always trending within each participant in the correct ordering of SF peaks (peak SF vs. surrogate SF, permutation test over participants, $p<0.001$).

We also checked the accuracy of SF estimation by using the technique on neurophysiological data with known SF characteristics, here MEG. The method successfully recovered the distribution of SF power previously reported for phase signal (**Figure 6B**; compare Figure 2 in Alexander et al. 2016, and Figure 2 in Alexander et al., 2019). Additional checks were made on the method using MEG data. **Figure 4** shows that each of the individual LSVs from SVD on MEG phase had different SF peaks using the method when computed separately, as expected from visual inspection of the LSVs (**Figure 3F**). This confirms that the peak SFs were being detected accurately, as the LSVs changed in SF characteristics. **Figure 6B** indicates how these separated curves sum to produce the completed SF spectrum in MEG.

However, we wanted to definitively rule out that the method was not just constructing distributions with left pointing tails, and that we were quantifying the left pointing tails as ~1/*f* spectra. To this end we constructed an MEG time-series of phase in which the high SFs dominated. This was achieved by reversing the order, and so the weighting, of the first *n* singular values and reconstituting the phase matrix according to eq. 2 (**Methods**) and as described in **Figure 2C**. **Figure 6C** shows that this surrogate data had a SF spectrum that increased monotonically with SF over the relevant range, i.e., the method accurately characterized the new SF spectrum.

To additionally rule out whether the produced SF spectra were an artefact of the sparsity and irregularity of the sEEG array, we produced MEG time-series of phase in which the sensors were randomly removed until the phase vectors were only one third their normal length, i.e., 51 sensors from an original 151. This procedure was repeated for several random removal sequences. The results are shown in **Supplementary Figure 5** and demonstrate that the effect of increasing measurement array sparsity and irregularity was to increase the noise of the SF estimate, as expected, but did not alter the overall shape of the spectra (wavelength vs. power, permutation test over runs, $p<0.001$). This procedure was repeated for the MEG surrogate in which high SFs dominated (i.e. SF power increasing with SF), with the same conclusions (wavelength vs. power, permutation test over runs, $p<0.001$).

We also tested for the effects of the average referencing used on the sEEG data (see **Methods**). Global synchrony appears as the DC component (SF=0) in spectra of phase. Computing an average reference increases the global synchrony of phase in an artefactual fashion. While this component is well separated from the minimum of the SF range of interest here, we needed to rule out the influence of the referencing method on our estimated spectra. To this end we produced spectra for MEG data, for which the case of a zero weight 'average reference' is also available (i.e., no reference). We compared spectra with an average

reference added at increasing levels influence. Increasing the weight of average reference up to a factor of eight times the usual average reference did not disturb the conclusions of this report (see **Supplementary Figure 6**). This procedure was tested with the methodological step that removed negative SF components (see **Methods**) and without. The results showed that this step both lowers the DC component of the SF phase spectrum—and thereby ameliorates the effects of any artefactual global synchronous component—but also does not introduce a false maximum at the relevant low SFs due to lowering of the DC component.

Cross-participant analysis

We analysed the relation between wavelength and estimated power for each participant using linear regression. The regression lines for the logarithm of wavelength versus estimated power are shown in **Figure 7**, for all individual participants at 9.2Hz (permutation test over participants, p<0.001). The regression lines for all TFs are shown in **Supplementary Figure 7** and all TFs showed a significant decrease in SF power with SF (permutation test over participants, p<0.001). The participants with the fewest triangles did not always show significant individual wavelength by SF power regressions at a given TF, but the regression lines almost universally trended (except one case) in the predicted direction. The present results extend the previous finding of ~1/f spectra in cortex (43,48) to temporal frequencies up to 100Hz.

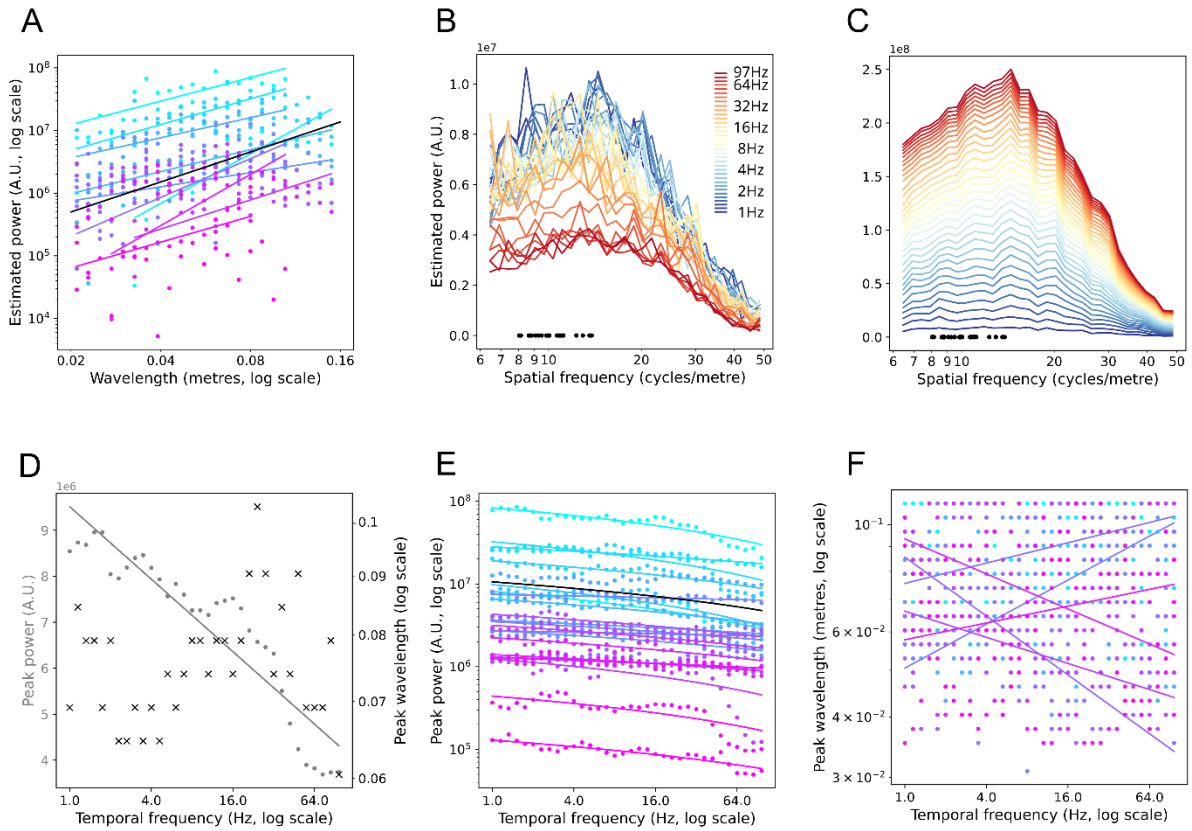

Figure 7. *Cross-participant analyses.* ***A****. Regression lines, for all participants, for wavelength versus SF power at centre TF 9.2Hz. Participants are ordered from most number of triangles (n=11051; light blue) to least number of triangles (n=56; lilac). Spectra values are shown as coloured dots (data from* ***Supplementary Figure 2****). Only individual regressions at 9.2Hz that were significant at p<0.05 are shown as regression lines. The mean slope and offset (of only significant regressions) is shown as a black line.* ***B****. Participant aggregate spectra for all TFs.*

TF is shown on the coloured scale. Individual lines are the mean spectra over 23 participants at that TF. The maximum triangle size (expressed as equivalent SF, i.e. 1/m) is shown for all 23 participants, as black dots. ***C****. The same spectra as* ***B****, except shown as a stacked histogram, giving the overall shape of the spectra.* ***D****. Regression of peak power versus TF (grey dots) and SF at peak power versus TF (black crosses; data from* ***B****). Significant regression line for peak power is shown in grey.* ***E****. Single participant regression lines for peak power versus TF. Colour conventions the same as* ***A****, and the mean slope and offset of the significant regressions is shown as a black line. Peak power is shown on a logarithmic scale for visualization purposes only.* ***F****. Single participant regression lines for SF at peak power versus TF. Colour conventions the same as* ***A****.*

The cross-participant analyses also confirmed that peak SF power declined linearly with increasing TF (logarithmic scale). This is show in **Figure 7D** for the participant-aggregate spectra (permutation test, $p<0.001$) and for the individual participant's spectra in **Figure 7E** (permutation test over participants, $p<0.001$). This effect may be wholly or in part due to measurement and quantification noise at higher TFs, as previously mentioned. Importantly, the cross-participant analyses revealed no effect for TF on SF at peak SF power. This was true for participant aggregate spectra (**Figure 7D**) and for the permutation test over all individual participant's regressions of (logarithm of) wavelength at peak SF power (**Figure 7F**). This means that the relative shapes of SF spectra were the same, regardless of TF. That is, the SF spectral power decreased monotonically over the relevant range from 8-12 to 50/cm, for TFs 1.0 to 100Hz.

The linear regressions we performed excluded SF estimates lower than the reciprocal of the maximum triangle size. This decision arises from considerations of Fourier analysis, in which the maximum wavelength detectable in broadband signal is a strict function of the maximum range of the (regular) grid size. In our results, the apparent SF power drops off for SFs lower than this, but this part of the spectrum is not meaningful. With the present method, maximum array size was weakly correlated with the SF at peak power for each participant (peak SF in TF aggregate spectrum vs. maximum inter-contact distance, permutation test, $p<0.05$, $r=0.31$). Maximum array size is defined by the two most (geodesically) distant contacts. It does not, therefore, always reflect the typical largest distances for the array. We describe in the **Methods** how peak SF is a function of the distribution of triangle sizes in irregular arrays and using the present SVD methods. For this reason, we use maximum triangle size as a bound for SF power regressions.

The array sizes used here did not reach the full extent of the cortex (~45cm), however, we were at the outset interested in the peak spatial frequency for the case where the array size extended to the entire cortex. For visual convenience, the regression lines in **Figure 5** and **Supplementary Figure 3** are extended to larger cortical distances. The linear relationship suggests that triangle sizes extending to the full range of the cortical sheet will result in peak SFs estimates larger than the maximum reported for the present participants. This prediction is supported by previous analyses using EEG and MEG, showing that the peak spatial frequency coincides with the size of the whole head array (11,30), which in turn coincides with the entire length of the cortex accessible over the upper half of the skull. It would be informative to repeat the analyses presented here after careful selection of sEEG participants from all available databases for maximum cortical sampling extent, or as technical advances in cortical sampling further improve. We expect that participants with greater than 30cm coverage will extend the linear trend reported here.

Effects of TF power

The main analyses all used phase as the input variable, reflecting our interest in cortical TWs. However, the main conclusions are not disrupted when TF power is included in the calculations. **Figure 8** shows the results when TF power is normalized on a contact-by-contact basis (see **Methods**). Individual participant's spectra are largely unchanged, with a suggestion of a weak increase in power at higher SFs (>30 cycles/m) compared to lower SFs (<10 cycles/m). **Supplementary Figure 8** shows the results of including (unnormalized) TF power. The clearest effect is the influence of decreasing TF power on SF power as TF increases (panels **A** and **B**) –TF power is small at higher TFs. We visually correct for this effect by plotting the relative values within the SF spectrum at each TF. Panels **C** and **D** show there is an apparent increase SF power between 12 and 20 cycles/m compared to the phase-only analyses, but not sufficient to overshadow the SF components 8-12 cycles/m. It is likely that much of this effect is due to noise in the measurement of signal amplitudes from contact to contact, since it largely disappears when power is normalized on a contact-by-contact basis. If a sensor array (e.g., a camera pixel array) is more sensitive at some sites than others, this will appear as an artefactual increase in higher SF components of the image.

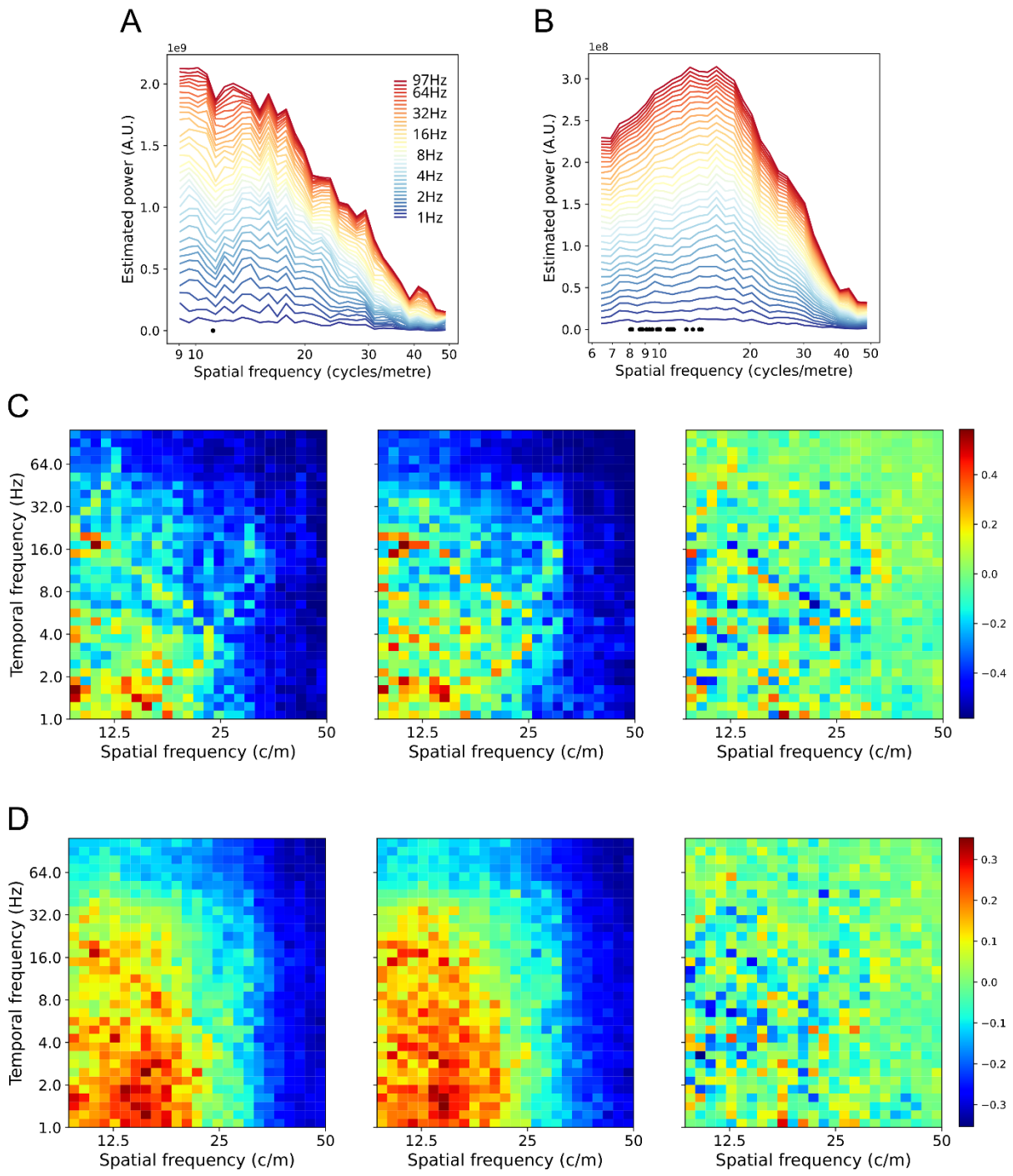

Figure 8. *Effects of including normalized TF power on SF spectra.* ***A****. Participant's stacked SF spectra with normalized TF power included in the estimate. TFs are shown on the colour scale. Compare with the same participant, phase only spectra,* ***Figure 5H****.* ***B****. Aggregate stacked SF spectra with normalized TF power included, over 23 participants. Compare with the aggregate stacked spectra shown in* ***Figure 7C****.* ***C****. Participant's SF spectra as SF by TF plot. The left plot shows the SF spectra with normalized TF power included (data taken from* ***A****). Power values are shown as colours, normalized between 0 (cold) and 1 (hot). The middle plot shows the phase only SF spectra (data taken from* ***Figure 5H****), normalized between 0 (cold) and 1 (hot). The right plot shows the difference between the two SF spectra, with differences given on the colour scale.* ***D****. Aggregate spectra for 23 participants, conventions the same as* ***C****. Data are taken from* ***B*** *and* ***Figure 7C*** *for the left and middle plots.*

Discussion

In this research we aimed to quantify the low SF part of cortical phase dynamics spectrum, up to the range of large-scale TWs (wavelength>8cm), using cortical depth electrodes. We developed a novel method to fill this important gap in our understanding of macroscopic phase dynamics, addressing a current limitation in the literature. Previous estimates have either relied on extra-cranial measurements (3,4,11,27,28,49) or used smaller measurement arrays (≤8cm) (2,6,31,33). This means either the results were biased by a low pass filter (due to volume conduction in EEG or distance to measurement array in MEG), or, had a maximum measurable SF below the large-scale range, respectively. We show that the spectral power increases with wavelength, up to the limit imposed by the maximum distances in the recording array. The present results are therefore consistent with the existence of large-scale TWs in the cortex (**Figure 1D**) and are inconsistent with the alternative hypotheses for the measurement of these waves extra-cranially (**Figure 1E & F**). Low SF activity dominates the cortical phase dynamics; most of the spatial power is at the longest wavelengths. In other words, most of the power measured extra-cranially is therefore produced by long wavelength activity in the cortex.

Considered from the perspective of locally measured phase—i.e., local to a single grey matter contact—the measured SF spectra imply that most of the variance in phase is a function of low SF phase dynamics. Note that this statement does not include cross-frequency effects, outside the (relatively broad) range of the frequency bandwidth of the phase estimator used in this study. The present result partly answers the longstanding question of why there is so much variability in locally measured cortical responses, even to the same stimulus (45, c.f. 46). We suggest that low SF phase dynamics index a distinct scale of cortical activity and, judged from their dominance of that activity, comprise an important scale for understanding cortical function (52). The variability is a mystery if the response in a functionally relevant area is considered in the absence of the global phase dynamic context. Our results suggest the variability can be controlled for if the global context is also measured.

The shape of the SF spectrum in the range ~8 to 50 cycles/m is therefore consistent with reports of the spectrum at smaller cortical scales (6,7,30). The cortical SF spectrum is generally described as $1/f^{\alpha}$, where the exponent α is a function of the type of measurement (e.g., grey matter, cortical surface or extra-cranial) (6,30,43). Since peak SF also increases with the total size of a participants' sEEG array (maximum inter-contact range), we assume that the $1/f^{\alpha}$ distribution of SF extends to the maximum size of the human cortex; this is approximately 45cm linear distance within the unfolded grey matter. This would be consistent with spectral peaks at lowest spatial frequencies measured using EEG (7,30) and MEG (11), since this is what is expected when a low pass filter is applied to a signal dominated by low spatial frequencies.

A surprising finding was that the shape of the SF spectrum did not vary much with TF. This finding implies that low SF cortical phase dynamics arise at temporal frequencies up to 100Hz, the maximum TF tested here. Some care should be taken in interpreting the SF spectra at temporal frequencies above 60Hz, since band-pass filtering alone is not sufficient to remove the low temporal frequency components of spiking activity (53). In addition, while volume conduction effects arise in local-field potentials (54), these are limited to 1cm range and so smaller than the minimum 2cm range (50c/m) reported here. These effects cannot explain the relatively uniform shapes of the SF spectra with changing TF.

Gamma (30-60Hz) and high gamma (>60Hz) synchrony have been functionally implicated across a range of scales in the cortex. Several studies have quantified the functional role of gamma band oscillations within cortical areas, notably in the visual and motor areas. Spike triggered analysis of local field potentials in V1 has shown that TWs have a greater range of propagation under low contrast visual stimulation, compared to high contrast (55). In multiple visual areas, Womelsdorf et al. (56) demonstrated that gamma phase synchrony between recording sites precedes high amplitude correlations between those same sites. V1 oscillations were analysed in the range 50-80Hz using the transfer entropy of the phase and show the activity to be compatible with directional wave propagation (57). Blakely et al., (58) analysed temporal covariance of gamma band activity recorded in ECoG arrays to map finger flexions in the motor cortex.

At a larger spatial scale, it has been demonstrated that the (putative) causal influence of frontal regions on more posterior zones using the phase slope index, across a wide range of temporal frequencies, including gamma (59). sEEG recording has been used to analyze long-range high frequency phase synchronization (60). Using zero- and nonzero-lag phase measures, these authors demonstrate that phase locking occurs in the high TF ranges 100 to 450Hz, across globally ranged cortical regions. None of these studies, however, specifically assessed the SF spectrum of the phase signals.

The existing literature on gamma-band TWs is patchy but consistent with our findings here. Macroscopic TWs are commonly reported in the delta to beta ranges (3,4,27,29,61). However, TWs have also been reported for low gamma frequency (40Hz) using MEG, in an event-locked paradigm (48). Similarly, EEG-based estimation of SF has been reported for temporal frequencies from 7 to 63Hz, with similar spectra ($1/f^{\alpha}$) for spatial frequencies over this entire range (43).

We outlined in the introduction the theory of cortical TWs as group waves (13,14,17), which means the group wave velocity can exceed the speed of information propagation. Specifically, the rise and fall of coordinated cortical activity can outpace axonal conduction times, since it depends on patterns of spikes that have previously arrived (23). If TWs are group waves and do not directly reflect the speed of information propagation, this may appear to support the argument that the cortex's electric fields are epiphenomenal, and that spiking activity of individual neurons is the ground truth. However, the literature on TWs shows that they can influence spiking patterns of individual neurons (33,53,54 cf. 35). To this we may add reports of the endogenous electro-magnetic field altering firing patterns of neurons (63,64). It seems likely that a major driver of cortical plasticity is precisely the dominant SFs found in the cortex, since post-synaptic membrane depolarization is the second major ingredient of long term potentiation (65). An evolutionary argument can also be applied, since dominant low SF phase dynamics will be more metabolically expensive than otherwise quiescent, mostly locally activated cortex. This implies critical function rather than epiphenomenon. Taken together, these arguments suggest that the pattern of phase organization in the cortex has a causal role and is not the epistemological equivalent of heat generated by a CPU.

The present results have important methodological implications. Considerations from Fourier analysis raised in the introduction indicate that the maximum spatial sampling range is critical to setting the lower bound of detectable SFs. This would not be the case if the SFs were pure and isolated, but for broadband, highly mixed signals it is. These considerations are supported empirically by the present results. The peak SF increases in wavelength with maximum contact distance for the participants (here, 0.12 to 0.24m), which in practice is related to the

number of contacts, and maximum triangle size used in the present methods. In addition, we showed that there was a linear relation between peak SF and the triangle size used to estimate SF. The present findings also explain why detected TWs, regardless of cortical scale, generally have a wavelength ~2π (29,66). If the spatial spectrum is monotonically decreasing in power over the entire large-scale to microscopic range, then the highest power waves detectable on the array will be those with a wavelength approximately the size of the array.

We conclude that reports of TWs should include estimates of SF to allow or disallow comparisons between studies with different extents of cortical coverage, since they may be accessing different SF ranges and therefore different functional connectivity ranges (c.f. 31,32). The present results, along with considerations from Fourier analysis, indicate that only methods that have large-scale coverage of cortical activity can assess the dominant scale of cortical phase dynamics. Unfortunately, source localization techniques, designed to improve upon sensor-level measurements, remove long range spatial correlations in the signal; both artefactual and real (18,68). This excludes these techniques from accurately estimating the SF spectra of phase dynamics since they filter out precisely the most dominant components, according to the present results. Similar considerations apply to methods to remove volume conduction effects from local field potential recording, such as taking the first- or second-order spatial derivatives.

For this reason, we argue, forward models of cortical activity are better suited to discovery of cortical dynamics from extra-cranial measurements (69–71). The present results suggest that the key methodological assumption of source localization techniques, namely that localized peaks in activity can be quantified to produce a mapping from extra-cranial patterns of activation to cortical locations, may not be sustainable. The contrary case, that high SF peaks exist in the cortical spectrum in real time (or that the low SF dominance is functionally irrelevant) should be demonstrated rather than implicitly assumed. Worse, confirmation of our present results would more broadly suggest that the endeavour itself is less meaningful than previously appreciated. If high SF activity forms only a small part of the total SF spectrum, then source localization is not just an ill-conditioned problem, but perhaps not the problem. At the least, estimates of relative amounts cortical activity explained, by sources thus localized, should be attempted (see 72,73 for some discussion of these issues).

TWs have been shown to allow prediction of future phase at single recording sites two wave cycles into the future. This effect was shown for both macroscopic MEG and ECoG (~8cm range) measurements (8). The ability of TWs to predict future local activity shows that the long-range spatio-temporal correlations inherent in the structure of low SF activity are functionally significant. Future research could extend this approach using high temporal resolution sEEG to detect individual spikes and to characterize large-scale phase dynamics and to predict the former from the latter. More generally, most of functionally-related results concerning large-scale TWs have been obtained using extra-cranial methods (27,28,49,61,74). The reported linkage between late event-related potentials and TWs (4,29,75,76) means the body of research into late event-related potentials can guide experimental verification of the functional significance of macroscopic TWs at the single trial level.

Our conclusions regarding the dominance of large-scale cortical activity are consistent with other recent findings in neuroscience. There has been a resurgence of interest into the global structure of the cortical functional map, driven by developments in fMRI, large-scale open-

access databases, and numerical analysis techniques (15,77,78). An intrinsic functional coordinate system has been proposed: along with hemispheric lateralization, a global coordinate axis has been described in terms of a visual to somatosensory/motor dimension, beginning at the occipital pole and calcarine sulcus, extending around the cortical hemispheres through the temporal lobe, frontal areas and to the central sulcus. Another dimension, at approximately twice the SF, is a function of the cortical distance between the primary areas and transmodal areas (77). Eigenmode analysis of fMRI data shows that macroscopic wavelengths dominate the spatio-temporal activity at time-scales characteristic of fMRI (15). This is consistent with previous findings in the EEG and MEG showing that long wavelengths are ubiquitous features of the spatio-temporal activity in the ranges delta to beta (27,29,31,67,79). Here, we have shown that low SF phase dynamics dominate the spatio-temporal organization of cortical activity measurable in the grey-matter, and that these global dynamics extend to fast cortical time scales into the high gamma range, at 10's of milliseconds.

Methods

Data acquisition

We summarize the relevant details of the RAM data set here (35; https://memory.psych.upenn.edu/RAM_Public_Data). Full details of data acquisition are reported elsewhere (80). 35 human participants were part of a multi-centre sEEG monitoring study. The participants were drawn from experiments 'FR5' and 'catFR5', and we included those that had complete data sets for present purposes (time-series, contact locations, cortical surface meshes). From the initial pool of participants, 23 had sufficient numbers of grey-matter contacts to enable further analysis (see Numerical methods for criterion). Mean age was 34 years, nine female, four left-handed.

The participants' task was designed to assess the effects of electrical stimulation on memory-related brain function. Each participant engaged in a delayed free recall task in which they studied lists of words for a later memory test. Trials with stimulation were not used in the present study, and our interest was in the general characteristics of cortical activity, not especially dependent upon this task. The research protocol was approved by the institutional review board at each hospital and informed consent was obtained from each participant. Electrophysiological data were collected from electrodes implanted within the brain parenchyma. Participants had temporal lobe depth electrodes, with frontal and parietal regions targeted as needed to best localize epileptogenic regions. Contacts on each electrode had a 5mm inter-contact spacing. The sampling frequency was 1000Hz, except for 8 participants, for which it was 500Hz. The number of grey-matter contacts ranged from 31 to 108 with a mean of 58.

The data for each participant was denoised by first calculating the standard-deviation of signal over samples, for each trial and sensor combination (44). If the mean standard-deviation for a trial was greater than ±3 the mean standard-deviations from all trials, then that trial was removed from further analysis. Then, if the mean standard-deviation (after recalculation) for a sensor was greater than ±1.5 mean standard-deviations from all sensors, it was removed from further analysis. Finally, if the standard-deviation (after recalculation) for a trial by sensor combination was greater than ±3 standard deviations from all trial by sensor combinations, it was replaced with the average signal (average calculated after excluding all over threshold trial by sensor combinations).

Using the automated contact labeling supplied within the dataset (checked and corrected manually by clinicians), contacts were partitioned into three groups: grey-matter, white-matter low-amplitude and other white-matter. We defined *white-matter low-amplitude contacts* as those whose standard deviation of signal amplitudes were in the bottom 50% of white matter contacts. The white-matter low-amplitude contacts were pooled to create an average reference for the grey-matter contacts (44). All numerical procedures were trialed using notch filters to remove the 60Hz line signal and its harmonics, and repeated without notch filters simply by avoiding these bands. No numerical differences were obtained for the common frequencies in the two versions of the data analyzed, so the former analyses are reported here.

Numerical methods

Phase estimation

Phase is represented as a unit-length complex number, ϕ.

$$\phi = e^{-i\theta};\ \{\theta \in \mathbb{R} \mid -\pi \leq \theta < \pi\} \qquad \text{eq. 1}$$

We used complex-valued phase (8,81,81) in conjunction with the complex SVD to avoid the (error) noise introduced by spatial unwrapping phase when using real-valued techniques (c.f. 2,4,26,36,37). Phase is calculated from the sEEG time-series, for a particular TF, using short time-window Morlet wavelets (2 cycles, (84)). Short time series methods were used because previous research has shown TWs to often last only one or two cycles, and windows of 5 or 7 cycles can wash out the detail of fast temporal changes (4). Use of short-time window Morlet wavelets increases the temporal resolution of the phase estimate, at the cost of a decrease in TF resolution. For example, the wavelet with centre TF at 4.5Hz has a half-power bandwidth spanning 2.5 to 6.8Hz. This lower TF resolution has positive consequences, since it makes the analyses here-in more robust to small variations in TF across areas and regions.

We estimated phase for 34 centre-TFs, logarithmically spaced from 1.0 to 97.0Hz. Due to the low TF resolution of the 2 cycle Morlet wavelets and number of frequencies extracted, this amounted to an oversampling of the frequency range. We use indices of *s* and *t* to refer to measurement sites and sample times, respectively, giving a matrix of complex-valued phases for each TF, $\mathbf{\Phi}_{st}$.

Because Morlet wavelets have poor frequency resolution, the very short time-window Morlet basis is only approximately sinusoid and robust to relatively wide variations in TF (85) and violations of sinusoidal shape. In practice, any surge of activity up and down with a time-course near the centre TF will have a high correlation with the applied Morlet basis. We are therefore confident that the present results are not confabulated by ‘ringing’ effects (86).

A potential criticism of the approach used here is that we estimate spatial frequency spectra for phase, while discarding amplitude information. The primary reason is our interest in TWs, which are generally defined in terms of phase. It is worth noting that single trial phase is a stronger determinant of mean signal amplitude than is single trial amplitude (29). This has been shown for EEG, MEG and ECoG. In other words, aggregate measures such as event-related potentials, coherence, and even values for the lead field matrix in beamformer techniques, are predominantly a function of phase interference over aggregated samples rather than true sample-by-sample variations in source amplitude (29,79). Conversely, if the amplitude recorded at contacts is sufficiently small, the estimated phase values will not affect the estimates of spatial frequency produced here; they will be noise-like and not contribute to the dominant components of the SVD. We introduce the effects of TF amplitude as an addendum to our main analyses.

SVD for empirical Fourier decomposition

Fourier methods are commonly used in scientific research to analyze signals that extend in time and space. The methods use sinusoids as a basis to decompose arbitrary n-dimensional series into weighted sums of sinusoids. Fourier methods have been used to analyze TWs in the EEG (3,87). The non-uniform spacing of the measurement array in the standardized

montage (e.g., 10-20 system) is overcome by interpolating a regular grid between measurement sites. In sEEG, however, the contact spacing is irregular to a much larger degree, making interpolation not an option. Fourier analysis with multi-resolution grids is still an active area of research (42,88), yet these approaches are limited to a few scales of grid and do not account for irregular sampling. The analyses provided by nonuniform discrete Fourier transform methods (37–39,41) are also not suited to the extremes of sparsity and irregularity of the grey-matter sEEG contacts analyzed here.

SVD is a standard method to reorganize data into a more interpretable form. SVD has recently become a more common tool in neuroscience (15,89–94); for an alternative view, see (46)). Here we used SVD primarily to discount the influence of phase estimates that do not contribute strongly to the spatial covariance of phase. Also, the LSVs can be interpreted as Fourier components with corrections for the irregularity of the measurement array.

We have previously shown that SVD can be used to decompose phase data obtained via EEG, MEG or ECoG (4,29). The measurement coordinates of the scalp EEG or MEG sensor array define the (partial) surface of a three-dimensional spheroid. The SVD decomposes the phase data into families of phase gradients projected onto the surface of the spheroid. As illustrated in **Figure 3F**, the first three LSVs extracted using SVD are approximately equal in wavelength to the size of the measurement array. Since the LSVs were smooth gradients of phase, this meant these first three components were large-scale TWs. The first three components were (for EEG) anterior-posterior gradient, inferior-superior gradient and left-right gradient (4). In addition, macroscopic TWs with arbitrary directions could be described using weighted sums of the components, e.g., a mixture of the anterior-posterior and left-right gradients gives a diagonally propagating macroscopic TW. The next three LSVs were approximately wavenumber equal to two (i.e., twice the spatial frequency), and each successive three LSVs increasing in wavenumber by one (29).

We can draw out the relation between SVD and Fourier analysis more explicitly. Consider phase data with a smooth spatial organization, where the peak in the spatial frequency spectrum is at long wavelengths (i.e., $\lambda \approx$size of measurement array), and the spectral power monotonically decreases with increasing spatial frequency. A matrix of a phase signals, **A**, then decomposes the many samples of spatial vectors of phase into a series of LSVs, u_r in descending order of singular values, σ_r, considering only the r highest singular values (95).

$$\mathbf{A} = \mathbf{U}_r \mathbf{\Sigma}_r \mathbf{V}_r^* = \sum_{i=1}^{r} \varsigma_i \mathrm{u}_{\boldsymbol{i}} \mathbf{v}_i^* \qquad \text{eq. 2}$$

The effectiveness of the SVD is that it re-organizes the data into components that are uncorrelated with each other (the LSVs), but that explain known amounts of variance in the data (the singular values). Because the correlation is zero, the components can be treated as independent observations of a system. Weighted sums of these components reproduce the original data in a lossless manner. Alternatively, only the most important components can be kept to more concisely describe the original data, while the ignored components can be treated as noise. One of the main reasons to use SVD in the present research is the reorganization of data into components that explain most of the variance, and others which are noise-like. This means the SVD discounts phase measurements that do not create consistent patterns of spatial covariation. This is a desirable effect, because being able to calculate phase at each

time-point and contact does not imply the phase is meaningful. By choosing a cut-off in the reduced-rank SVD model that excludes negligible sources of explanatory variance, the meaningless measurements of phase are excluded. This would not be the case if spatial frequency estimates were made directly on the phase estimates.

SVD has been described as a generalization of Fourier analysis (96), in that it is used to empirically recover a set of bases that allow the original data to be represented as weighted sums of that basis. We illustrate in **Figure 3** that analysis of suitable signals using SVD enables recovery of a set of bases that are approximations of sinusoidal basis functions, (see also (46) for a critical view). 'Suitable' here means (a) monotonically decreasing in power with frequency or calculated at a clear peak in the power spectrum, (b) containing no other strongly competing explanatory features (such as gradients) and, importantly, (c) smoothness of values in the underlying function. Suitable signals include digitized classical music, noise generated by random walk processes (proof in Shinn 2023) and intra- and extra-cranial cortical measurements (8,79). This specific ability of SVD to recover approximately sinusoidal bases means that, though empirically driven, in the present research there is a close theoretical relation between SVD and Fourier analysis.

The reasons that SVD finds a sinusoidal basis are treated in Shinn (2023), for the case of a uniform measurement array. Essentially, spatial smoothness in the signal means neighbouring values quantify the curvature in the form a central difference approximation of the second derivative. In the present data, the spatial smoothness is a function of real correlations in cortical activity across space, plus short-range volume conduction (<1cm; 91). The continuous function corresponding to this difference approximation is the harmonic oscillator, which is satisfied by linear combinations of sines and cosines. Depending on the boundary conditions of the signal, the SVD components may also involve the first order forward finite difference approximation of the first derivative. Here also, the corresponding function in the continuous case is also a sinusoid. Also depending upon the boundary conditions, the LSVs may not be pure Fourier components but weighted sums of the terms in the Fourier series (46).

In the present research, the vectors of phase (over the array) were decomposed into uncorrelated components using SVD. The matrix of complex-valued phases, $\mathbf{\Phi}_{st}$, is submitted to the SVD. Two outputs from the SVD are used to compute the SF spectrum. These are the LSVs, which are each complex-valued vectors with indexes *s*. Each value within an LSV, $\boldsymbol{\zeta}_s$, consisted of a phase, $\boldsymbol{\omega}_s = \angle\boldsymbol{\zeta}_s$, and a magnitude, $\boldsymbol{a}_s = |\boldsymbol{\zeta}_s|$, which could vary over the LSV, e.g. $\boldsymbol{a}_s$ tend to be low at singularities (rapid rates of change) in $\boldsymbol{\omega}_s$. The second output, the LSV scaling value, $\boldsymbol{\varsigma}_r$, is obtained from the main-diagonal values of the scaling matrix $\mathbf{\Sigma}_r$, and comprises the ordered contributions, or weightings, of each LSV's contribution to the original data.

Subsequent to the SVD, it is crucial to analyze the nature of the components, rather than just assume they are physically meaningful decompositions of the measurements (98). This reality check arises the same sense for Fourier analysis, which is guaranteed to decompose any continuous signal into sums of sinusoids, even if the underlying physical process is not sinusoidal, such as in heat diffusion (99). Here we use the SVD as a preliminary step to then estimate the spatial frequency spectrum in sEEG, rather than make specific claims about the empirical meaningfulness of the components, although related methods and claims have been used in a wide range of neuroscience research (15,89–93).

The threshold for exclusion of 'noise' components is justified by the wide range of dimension reductions (between 10 and 40 components) that were trialed. The method does not depend on choosing a particular number of signal components. The noisier the component (from the point of view of spatially coherent patterns of phase), the lower its contribution to variance explained by the SVD (and hence to the SF calculation). In the results reported here we used the first 14 LSVs and singular values.

Here, we describe in more detail the relation between Fourier analysis and SVD methods to introduce the logic of the method. We limit our description to the one-dimensional case, without loss of generality. For suitable signals, as defined earlier in this section, each of the first few LSVs, v_k, is an approximate complex sinusoid with wavenumber equal to *k*.

$$v_k \cong e^{-i2\pi k} \qquad \text{eq. 3}$$

This means the SVD has decomposed the matrix of complex-valued phase into bases that approximate a Fourier decomposition in the spatial dimension

$$\boldsymbol{\psi}_{\mathrm{k}} = \sum_{n=0}^{N-1} \psi_n \cdot e^{-\frac{i2\pi}{N}kn} \qquad \text{eq. 4}$$

where Σ_n is the sum over the spatial array of length N samples. Note that this means the maximum spatial frequency that can be measured is equivalent in size to a one cycle sinusoid (i.e., when *k*=1) over the sampling array.

Just as the LSVs play the same role as the last term in equation 4, $e^{-\frac{i2\pi}{N}kn}$, so the singular values describe the weights of each sinusoidal term, corresponding to the sums over ψ_n in Fourier analysis. The spatial frequency spectrum can therefore be estimated after the SVD by summing over the singular values assigned to unique (or by binning over a limited range of) spatial frequencies. This procedure is illustrated in **Figures 3** and **4**.

This correspondence, between Fourier analysis and SVD of spatially organized phase, allows spatial frequency spectra to be estimated on semi-regular arrays, such as EEG, MEG as well as ECoG arrays on the surface of the cortex (8,11,29). The first dozen or so LSVs can be assigned a spatial frequency by calculation of the circular range of phase across the array. This assignment is possible because the maps of phase so-produced are smooth and regular, even if the measurement array is semi-regular (11,29). Note that the smooth maps of phase arise from the regularities (covariances) in the phase data itself, and do not require information about the spatial locations of the measurement sites. The measurement locations are only required, *post hoc*, to estimate the spatial frequency of the maps, in cycles/m.

We hypothesized from our previous observation regarding LSV of phase (4,11,29) that the methods would generalize sufficiently well to estimate SF spectra in the case of highly irregular measurement arrays. Ruiz-Antolin & Townsend (41) show that Fourier analysis can be performed on non-uniform arrays, provided each (irregularly placed) sampling site can be re-mapped to a sampling site on a uniform array. The key observation to their procedure is that the effects of the re-mapping can be well approximated as a low rank matrix, and these effects can be computed by a limited number of additional, corrective, Fourier analyses. It seems reasonable then to assume that, just as SVD captures sinusoidal components on (quasi-)

regular arrays, SVD can also capture components on highly irregular arrays that are combinations of sinusoidal and the (low-rank) effects of sampling site-displacement. Such a mathematical proof is beyond the scope of the present research. Instead, we rely on surrogate testing to show that the present method accuracy assesses the shape of the SF spectra. We discuss this issue further at the end of the **Methods** section.

Removal of DC component of phase spectrum

Alexander et al. (2016) introduced a quantitative method for splitting spatio-temporal waves into positive and negative components. This enables the pure TW component to be measured, while removing the effects of standing wave activity, including global phase-locked synchrony. We apply this method to the LSVs of phase to account for the effects of average reference, which introduce an artifactual global synchrony, thereby inflating the lowest SF's power. Since we are considering the spatial spectra of phase, the removal of globally synchronous components has the effect of removing the DC component of the spectrum. In general, this component is outside the range of SFs of interest here (8 to 50 c/m), and inclusion or exclusion of this methodological step did not influence the present findings. It allowed us never-the-less to discount the DC component in the phase spectrum.

The positive SF component is calculated as follows. The procedure takes vector of Fourier components (phase-only or including the amplitude) over the array. Specifically, the LSVs are used as input to this algorithm. The LSV, which has complex magnitude and phase, $r\phi_s$, is first extended to one full cycle of phase

$$r\phi_{sc} = r\phi_s \times \phi_c \qquad \text{eq. 5}$$

where × is the Cartesian product, ϕ_c is a vector of unit length phases over *n* samples, where

$$n = \lfloor f_s/f \rceil \qquad \text{eq. 6}$$

and f_s is the sampling frequency and *f* is the centre frequency of the phase estimate. We then perform an SVD on the real part of the temporally extended phase vector. The pure TW can then be estimated combining the first and second LSVs into the real and imaginary parts of a complex-valued phase vector

$$\phi_p = e^{-i\angle(u_1+iu_2)} \qquad \text{eq. 7}$$

where *u* are the LSVs of $\mathbb{R}(r\phi_{sc})$. Examples of the LSVs of $\mathbf{\Phi}_{st}$ for the MEG data, before and after the removal of standing wave effects, are shown in Supplementary Figure 9.

Multi-scale differencing of phase

For the sEEG, the extreme irregularity of the array means the smoothness of the phase in the LSVs of $\mathbf{\Phi}_{st}$ breaks down. To overcome this limit, we introduce further numerical analyses based on multi-scale differencing. We used multi-scale difference methods since we were interested in estimating the entire spatial frequency spectrum, including global ranges. The accuracy of the multi-scale differencing method was compared to SF spectra obtained using an alternative measurement modality (MEG) and using surrogate data whose ground truth

was known by construction. Surrogate testing indicated that use of nearest neighbour differences alone was not sensitive to lower SFs known to be present in the data. Further, we demonstrate an important effect of the distortions introduced by the irregularity of sEEG contacts to smooth phase maps calculated via SVD. These distortions meant the largest inter-contact distances were most sensitive to low SF parts of the signal and the smallest contact distances were most sensitive to high SFs. This observation differs from smooth wave maps (4,29), such as those obtained from MEG (**Figure 3F**). Smooth wave maps provide the same estimates of rate of change of phase per metre at all spatial scales of differencing, because of their uniform rates of change in phase with distance.

The SF contributions of each LSV were quantified by considering of triplets of phase values, in the form of approximately equilateral triangles mapped onto the folded cortical surface. The rate of change of phase per metre, across triangles of contact sin each LSV, was used for each estimate of spatial frequency. The results therefore did not directly require the inference of spatial oscillatory components (98).

We group contacts into approximately equilateral triangles so the direction of phase flow could be unambiguously determined. Comparing phase between pairs of contacts, such as in phase coherence (18,100), along a line of contacts (3,26,27), or for a highly elongated triangle, only measures the phase flow along the axis in which the contacts are aligned. This procedure can greatly overestimate the rate of change of phase, in the case where the flow has a strong orthogonal component, i.e., is directed across the axis on which the contacts are arranged. We therefore re-organize the irregular field of sensors into triplets of approximately equilateral triangles.

We collated the unique triangles, i.e., contacts could appear in multiple triangles. First, the contact's position was projected to the nearest point on the surface of the cortex. We then computed the geodesic distance (47) between every pair of contacts using the surface mesh derived from the participant's MRI scan. Triangles were counted as approximately equilateral if the most acute angle was greater than π/4. Calculating geodesic distances enabled the true distances along the surface of the cortex to be accounted for and, since the TWs move through the cortical sheet, this is presumed more accurate than taking the Cartesian distances from the folded cortex. Use of the geodesic distance measure—which is only defined within a hemisphere—also meant the triangles were only defined within hemispheres, i.e., a triplet of contacts could not span both hemispheres. Contacts in the sEEG participants often exist in both hemispheres. However, the SVD step allowed patterns of phase to be detected from the regularities (covariances) across hemispheres. Examples of geodesically defined triangles are shown in **Figure 5** and **Supplementary Figure 1**, from both large and small size triangle bins.

The number of triangles varied from 11051 down to 66 across participants, resampled from a range of grey-matter contacts 108 down to 31. Triangle spatial frequency, ξ_T, is given by one over the triangle linear size (square-root of the area of the triangle):

$$\xi_T = 1 \Big/ \sqrt{|\overline{\mathbf{AB}} \times \overline{\mathbf{CA}}|/2} \qquad \text{eq. 8}$$

$\overline{\mathbf{AB}}$ and $\overline{\mathbf{CA}}$ are edge vectors of the triangle with vertices *A*, *B*, *C* and × is the cross-product. *A* is nominally at coordinate (0,0) within the triangle, and *B* and *C* are computed via the relevant geodesic distances across the cortical sheet. The spatial frequency distribution of triangle sizes formed a peaked distribution with maximum triangle counts occurring near the large end of triangle size range (see Supplementary Figure 1). An effective uniform distribution of ξ_T was achieved by dividing the range of ξ_T into 32 equally spaced spatial frequencies, corresponding to triangle sizes from 32cm to 1cm. An additional bin with the smallest triangle sizes was allowed to include the rare triangles of size <1cm and, depending on the participant, the lowest ξ_T bins could be empty if the contacts spanned a more limited range than 16+cm. A normalization term, N_T was then applied, such that the weight of each triangle's contribution to the SF calculation was inversely proportional to the number of triangles in that triangle's bin. This meant the SF estimates of phase were undertaken using an underlying set of distances with an effective uniform distribution in ξ_T.

For each LSV, and for each triangle of three contacts, we computed the rate of change in phase per metre on the triangle in the abstracted plane implied by the three inter-contact geodesic distances. Hence the spatial frequency, ξ, is given by:

$$\xi = \frac{|\boldsymbol{\omega}\nabla_H|}{2\pi} \qquad \text{eq. 9}$$

where ∇_H is the horizontal (i.e., two dimensional) del-operator, so

$$\boldsymbol{\omega}\nabla_H = \begin{bmatrix} \frac{\partial \boldsymbol{\omega}}{\partial x} \\ \\ \frac{\partial \boldsymbol{\omega}}{\partial y} \end{bmatrix} \qquad \text{eq.10}$$

and $\boldsymbol{\omega} = \angle\boldsymbol{\zeta}$. Each vector in eqs. 9 and 10 has an implicit triangle index, *T*, which indexes a triple of contacts drawn from *s*, and LSV index, *r*, so ξ can be rewritten as ξ_{rT}.

The weighting of each triangle's contribution to the spatial frequency spectrum is computed as a function of the scaling value of the rth LSV (i.e. the amount of variance explained), the magnitude of the LSV's complex-value at the triple of relevant contacts and the normalization term for each triangle, and is given by:

$$\mathbf{W}_{rT} = \boldsymbol{\varsigma}_r \langle \boldsymbol{a} \rangle_T N_T \qquad \text{eq.11}$$

where $\langle \boldsymbol{a} \rangle_T$ is the mean element-wise magnitude of $\boldsymbol{\zeta}_s$ for the subset of three vertices in *s* for LSV *r*. Combining the spatial frequency estimate for each geodesic triangle in each LSV (eq. 9), with the weighting of each triangle's contribution to the power (eq. 11), allows the construction of the estimated spatial frequency spectrum. For *K* SF bins, we have a bin width, *w*:

$$w = \left\lceil \frac{\max(\xi) - \min(\xi)}{K} \right\rceil \qquad \text{eq. 12}$$

with each ith weight $\mathbf{W}_{rT}$ being assigned to the bin corresponding to its the computed i^{th} SF, ξ_{rT}. The estimated power in arbitrary units (A.U.) for the kth bin, $k \in [1, K]$ is then,

$$P_k = \sum_i \mathbf{W}_i \,;\, i \in \{j \mid kw \leq \xi_i < (k+1)w\} \qquad \text{eq.13}$$

We used 32 SF bins to plot the SF spectra, after choosing $\min(\xi)$ and $\max(\xi)$ on a reasonable range (e.g. SFs equivalent to twice the maximum triangle size through to 50c/m for plotting the sEEG data; SFs equivalent to the maximum triangle range through to 50c/m for computing regression lines). For some additional analyses, e.g. the effects of average referencing on the spectrum, the lowest SF plotted was 0.5c/m. The estimated power is in arbitrary units because it is a function of the number of contacts submitted to the SVD and number of components retained. Since these are both constant for the calculation of a given spectra, the relative power and different SFs is the relevant quantity for each participant.

Surrogate testing

The primary method of surrogate testing introduced an artificial SF component to the sEEG signal, whose ground truth was known. The artificial SF components were created by inflating the cortical mesh of each participant to a sphere, then projecting a phase gradient onto the sphere, in either the anterior-posterior or left-right directions. The phase gradients were varied in wavelength from 2 to 16 c/m, and the positions of the actual contacts projected onto the inflated sphere used to infer surrogate basis vectors. Surrogate right singular vectors (i.e. time-series of weightings for the LSVs) were constructed by reversing the time-order of the empirical right singular vectors for that participant at the relevant TF, then taking the complex conjugate to re-establish the correct direction of phase change over time. A surrogate time series in complex-valued phase was constructed using each surrogate basis vector as LSV, a scaling value of 1.0 and a surrogate right singular vector, according to eq. 2. The surrogate time-series in phase was added to the empirical phase signal at each TF, with the surrogate signal weighted, as w_{sur}, across a range of values to both (1) perturb the empirical signal (1/3 surrogate to 2/3 signal ratio), and (2) to see the effects of perturbation by realistic signals on the veridical surrogate phases (7/8 surrogate to 1/8 signal ratio).

$$\Phi_{sur} = e^{-i\angle(\Phi + w_{sur}\Phi_\xi)} \qquad \text{eq. 14}$$

where Φ_ξ is the phase surrogate signal at some SF and direction and Φ_{sur} is the combined signal.

We additionally analyzed two participants from a different, MEG, data-set (101), as a source of neurophysiologically realistic time-series with known SF spectra (Alexander et al., 2016). Surrogate testing of the method using MEG was included because the large number of quasi-regularly spaced contacts enables recovery of smooth wave maps using SVD, with visually apparent SF values for each map. We then used the present methods estimate the distinct frequency spectra for each individual LSV. In addition, we constructed MEG surrogates using the first 28 LSVs of phase, but reversing the relative weighting of the singular values, i.e. ς_i, in eq. 2. This produced an MEG surrogate signal, in which small spatial scales of activity dominated the signal, called hereafter the *f spectrum* (as opposed to the usual 1/f spectrum). We additionally made use of the large number of contacts in the MEG array to test the effects of sparsity of measurement contacts. The phase data for the f spectrum surrogate, along with the unmodified MEG phase data, were further evaluated by randomly removing subsets of contacts until only 1/3 remained (51 of 151). This analysis took advantage of the large number of sensors available with MEG, so that highly irregular arrays are constructed by increasing

the sparsity. This analysis was to rule-out that the estimated SF spectra were artefactually created by the sparsity of the sEEG arrays, when analyzed using our method. We also used these MEG time-series to test the effects of an average reference on our method, since with MEG the case of no reference is also available to analyze.

Effects of TF power

The main analyses here were undertaken using complex-valued phase but generalize naturally to complex values that are not unit length e.g. by not excluding TF power. Each value computed by the Morlet wavelet is denoted $r\phi = re^{-i\theta}$ where *r* is the power of the signal. The matrix $\mathbf{R\Phi}_{st}$ was submitted to the SVD, and the SF spectra estimated. There is inherent noise in the TF power, mostly due to the accuracy and residual uncertainty of contact placement relative to the *mm* scales of the cortical sheet. This results in large variation in the mean amplitude signal across contacts. For this reason, we also computed the normalized power at each contact, $\bar{r}$, such that the normalized power at a given contact varied between zero and one over the recording, and $\bar{\mathbf{R}}\mathbf{\Phi}_{st}$ was submitted to the SVD.

Statistical analysis

Statistical testing of linear regressions reported in the results was undertaken as correlation between the empirical values (y) and the regression model values ($\hat{y}$). For regressions of SF versus estimated power, linear fits of the model, $\boldsymbol{\rho}$, were undertaken using a log-log scaling of wavelength (1.0/SF) with power. This combination produced the best linear fits. The statistical significance of these correlations, over multiple comparisons, was tested by permutation methods. Each permutation of the data comprised a correlation between ys in the regression, and random shuffling of $\hat{y}$s (10,000 permutations). The probability of arriving at a mean correlation (ignoring the sign of the mean), $\langle\boldsymbol{\rho}\rangle_n$, over *n* frequencies, participants or other analysis dimension was compared to the actual (unsigned magnitude of the) mean correlation (i.e., a two-tailed test). The tests for the significance of a family of regressions are reported as "variable A versus variable B (permutation test over n-condition, p-level)". The p-level was set to $p<0.05$ for planned analyses (individual participant regressions of wavelength versus power, over all temporal frequencies) and $p<0.001$ for others. When *n* was one, i.e., only one correlation rather than the mean of a group of correlations, this is indicated by omission of the n-condition term.

Effects of triangle size on SF estimates

We have assumed that the LSV derived from irregular arrays can be understood as Fourier components along with low rank 'corrections' for contact displacements (41). As part of our methodological approach to apply multi-scale difference estimates of SF, we examined peak SF as a function of triangle size. Examination of SF spectra revealed that triangle bin size and SF peaks derived from each bin had a strong linear relationship. That is, small triangles were more sensitive to high SFs, large triangles were more sensitive to low SFs. Statistical analysis of spectra produced from each separate triangle size bin showed that triangle size (as mean triangle size over a bin) linearly increased with the peak in the SF spectra for that bin size (as logarithm of wavelength; permutation test over participants, $p<0.001$). Examples of this effect are shown in **Supplementary Figure 10**. This effect is not expected under standard Fourier analysis on regular grids, for which the SF estimates will not vary if calculated by difference

methods at alternative values for delta-distance. Likewise, the SF estimates from standard Fourier analysis will not substantively differ at most (except highest) SFs if the data are sampled with different underlying but uniform contact spacings. This effect arises in the present sEEG data due the irregular spacing of the contacts, which become encoded in the LSVs of the SVD.

We analyzed this effect with surrogate methods, manipulating the inputs to the SVD of the random walk surrogate shown in **Figure 2A**. We performed the same SVD while systematically changing the distribution of intercontact distances in the measurement array. The results are shown in **Supplementary Figure 11**. A sparse, uniform array, covering the same spatial range as our first analysis, retrieved the same SF components (panel **F**, column 1). A dense array with a narrow range of contacts retrieved only high SF components (panel **F**, column 5), relatively speaking, but exactly the components defined by the maximum array size. These results are expected from considerations from standard Fourier analysis. Intermediate cases of grid spacing were produced via modulo rearrangements of the contacts (102). The maximum contact range and the Nyquist frequency was varied systematically between the two extremes. Careful visual inspection indicates that SVD produced LSVs with high SF components that were a function of the minimum intercontact distance; this is shown by the rate of change of values in the LSVs in runs of nearest neighbour contacts (panel **F**, columns 2-4). However, lower SFs representations were also present in the extracted components; this is demonstrated by interpolating between equivalent points in each run of nearest neighbour contacts (panel **G**).

Consider the application of a simplified, one-dimensional version of the present methods i.e. estimating SF spectra from the LSVs via multi-scale contact distances rather than triangle sizes. When using a multi-scale contact array, the highest SFs can be extracted from smallest neighbouring intercontact distances. The lowest SFs can be extracted from the largest intercontact distances. This effect arises from the way the SVD reorganizes the Fourier information under conditions of non-uniform sampling (cf. Ruiz-Antolin & Townsend, 2018). This is the same effect we see for triangle size in the sEEG data, i.e. small triangles are sensitive to high SFs and large triangles to low. We therefore used multi-scale differencing to estimate the SF spectra, in order to capture the full range of SF information present in each LSV. The accuracy of this approach was then confirmed by the surrogate testing of the methods.

Acknowledgments

This project has received funding from the European Research Council (ERC) under the European Union's Horizon 2020 research and innovation programme (grant agreement No 852139 – Laura Dugué).

We want to thank to Dr. R. Austin Benn for helpful advice on measuring geodesic distances in the cortex, and to Dr. Kirsten Petras for reading versions of the manuscript and providing useful feedback.

Code availability

The key Python routines used in this research can be found here:

https://github.com/DugueLab/Traveling-wave-analysis/blob/main/estimation_of_SF_of_phase_of_cortical_activity_on_irregular_measurement_arrays.ipynb

References

1. Goldman S, Santelmann WF, Vivian WE, Goldman D. Traveling Waves in the Brain. Science. 1949 May 20;109(2838):524.

2. Zhang H, Watrous AJ, Patel A, Jacobs J. Theta and Alpha Oscillations Are Traveling Waves in the Human Neocortex. Neuron. 2018 June 27;98(6):1269-1281.e4.

3. Alamia A, Terral L, D'ambra MR, VanRullen R. Distinct roles of forward and backward alpha-band waves in spatial visual attention. eLife. 2023 Mar 6;12:e85035.

4. Alexander DM, Trengove C, Wright JJ, Boord PR, Gordon E. Measurement of phase gradients in the EEG. J Neurosci Methods. 2006 Sept 30;156(1):111–28.

5. Fakche C, Dugué L. Perceptual Cycles Travel Across Retinotopic Space. J Cogn Neurosci. 2024 Jan 1;36(1):200–16.

6. Barrie JM, Freeman WJ, Lenhart MD. Spatiotemporal analysis of prepyriform, visual, auditory, and somesthetic surface EEGs in trained rabbits. J Neurophysiol. 1996 July;76(1):520–39.

7. Ramon C, Holmes MD. Spatiotemporal phase clusters and phase synchronization patterns derived from high density EEG and ECoG recordings. Curr Opin Neurobiol. 2015 Apr;31:127–32.

8. Alexander DM, Ball T, Schulze-Bonhage A, Leeuwen C van. Large-scale cortical travelling waves predict localized future cortical signals. PLOS Comput Biol. 2019 Nov 15;15(11):e1007316.

9. Prechtl JC, Bullock TH, Kleinfeld D. Direct evidence for local oscillatory current sources and intracortical phase gradients in turtle visual cortex. Proc Natl Acad Sci U S A. 2000 Jan 18;97(2):877–82.

10. Bhattacharya S, Brincat SL, Lundqvist M, Miller EK. Traveling waves in the prefrontal cortex during working memory. PLOS Comput Biol. 2022 Jan 28;18(1):e1009827.

11. Alexander DM, Nikolaev AR, Jurica P, Zvyagintsev M, Mathiak K, Leeuwen C van. Global Neuromagnetic Cortical Fields Have Non-Zero Velocity. PLOS ONE. 2016 Mar 8;11(3):e0148413.

12. Grabot L, Merholz G, Winawer J, Heeger D, Dugué L. Computational modeling of traveling waves using MEG-EEG in human. J Vis. 2022 Dec 5;22(14):3511.

13. Nunez PL. The brain wave equation: a model for the EEG. Math Biosci. 1974 Dec 1;21(3):279–97.

14. Wright JJ, Robinson PA, Rennie CJ, Gordon E, Bourke PD, Chapman CL, et al. Toward an integrated continuum model of cerebral dynamics: the cerebral rhythms, synchronous oscillation and cortical stability. Biosystems. 2001 Nov 1;63(1):71–88.

15. Pang JC, Aquino KM, Oldehinkel M, Robinson PA, Fulcher BD, Breakspear M, et al. Geometric constraints on human brain function. Nature. 2023 June;618(7965):566–74.

16. Born M, Wolf E. CHAPTER 1 - BASIC PROPERTIES OF THE ELECTROMAGNETIC FIELD. In: Born M, Wolf E, editors. Principles of Optics (Sixth Edition) [Internet].

Pergamon; 1980 [cited 2024 Apr 4]. p. 1–70. Available from: https://www.sciencedirect.com/science/article/pii/B9780080264820500086

17. Nunez PL, Srinivasan R. A theoretical basis for standing and traveling brain waves measured with human EEG with implications for an integrated consciousness. Clin Neurophysiol. 2006 Nov 1;117(11):2424–35.

18. Srinivasan R, Nunez PL, Silberstein RB. Spatial filtering and neocortical dynamics: estimates of EEG coherence. IEEE Trans Biomed Eng. 1998 July;45(7):814–26.

19. Liley DTJ, Alexander DM, Wright JJ, Aldous MD. Alpha rhythm emerges from large-scale networks of realistically coupled multicompartmental model cortical neurons. Netw Comput Neural Syst. 1999 Jan;10(1):79–92.

20. Wright JJ, Sergejew AA, Liley DT. Computer simulation of electrocortical activity at millimetric scale. Electroencephalogr Clin Neurophysiol. 1994 May;90(5):365–75.

21. Orczyk JJ, Kajikawa Y. Magnifying traveling waves on the scalp. Brain Topogr. 2022 Jan;35(1):162–8.

22. Hindriks R, van Putten MJAM, Deco G. Intra-cortical propagation of EEG alpha oscillations. NeuroImage. 2014 Dec;103:444–53.

23. Skarda CA, Freeman WJ. How brains make chaos in order to make sense of the world. Behav Brain Sci. 1987 June;10(2):161–73.

24. Rosen BQ, Halgren E. An estimation of the absolute number of axons indicates that human cortical areas are sparsely connected. PLoS Biol. 2022 Mar;20(3):e3001575.

25. Zhigalov A, Jensen O. Perceptual echoes as travelling waves may arise from two discrete neuronal sources. NeuroImage. 2023 May 15;272:120047.

26. Burkitt GR, Silberstein RB, Cadusch PJ, Wood AW. Steady-state visual evoked potentials and travelling waves. Clin Neurophysiol Off J Int Fed Clin Neurophysiol. 2000 Feb;111(2):246–58.

27. Ito J, Nikolaev AR, Leeuwen C van. Spatial and temporal structure of phase synchronization of spontaneous alpha EEG activity. Biol Cybern. 2005 Jan 1;92(1):54–60.

28. Klimesch W, Hanslmayr S, Sauseng P, Gruber WR, Doppelmayr M. P1 and traveling alpha waves: evidence for evoked oscillations. J Neurophysiol. 2007 Feb;97(2):1311–8.

29. Alexander DM, Jurica P, Trengove C, Nikolaev AR, Gepshtein S, Zvyagintsev M, et al. Traveling waves and trial averaging: The nature of single-trial and averaged brain responses in large-scale cortical signals. NeuroImage. 2013 June 1;73:95–112.

30. Freeman WJ, Holmes MD, Burke BC, Vanhatalo S. Spatial spectra of scalp EEG and EMG from awake humans. Clin Neurophysiol. 2003 June 1;114(6):1053–68.

31. Woolnough O, Forseth KJ, Rollo PS, Roccaforte ZJ, Tandon N. Event-related phase synchronization propagates rapidly across human ventral visual cortex. NeuroImage. 2022 Aug 1;256:119262.

32. Rubino D, Robbins KA, Hatsopoulos NG. Propagating waves mediate information transfer in the motor cortex. Nat Neurosci. 2006 Dec;9(12):1549–57.

33. Eckhorn R, Gail A, Bruns A, Gabriel A, Al-Shaikhli B, Saam M. Neural mechanisms of visual associative processing. Acta Neurobiol Exp (Warsz). 2004;64(2):239–52.

34. Zanos TP, Mineault PJ, Nasiotis KT, Guitton D, Pack CC. A sensorimotor role for traveling waves in primate visual cortex. Neuron. 2015 Feb 4;85(3):615–27.

35. Cohen MX. Analyzing Neural Time Series Data: Theory and Practice [Internet]. The MIT Press; 2014 [cited 2024 Apr 3]. Available from: https://direct.mit.edu/books/book/4013/Analyzing-Neural-Time-Series-DataTheory-and

36. Orsher Y, Rom A, Perel R, Lahini Y, Blinder P, Shein-Idelson M. Sequentially activated discrete modules appear as traveling waves in neuronal measurements with limited spatiotemporal sampling. eLife. 2024 Mar 7;12:RP92254.

37. Margrave GF, Ferguson RJ. Wavefield extrapolation by nonstationary phase shift.

38. Candes E, Demanet L, Ying L. A Fast Butterfly Algorithm for the Computation of Fourier Integral Operators [Internet]. arXiv; 2008 [cited 2025 July 13]. Available from: http://arxiv.org/abs/0809.0719

39. Ying L. Sparse Fourier Transform via Butterfly Algorithm. SIAM J Sci Comput. 2009 Jan;31(3):1678–94.

40. A SVD-GFD Method to simulate 3D Moving Boundary Flow Problems [Internet]. [cited 2025 July 13]. Available from: https://scholarbank.nus.edu.sg/entities/publication/f06f4b66-f665-4ca1-a620-360da5389c87

41. Ruiz-Antolín D, Townsend A. A Nonuniform Fast Fourier Transform Based on Low Rank Approximation. SIAM J Sci Comput. 2018 Jan;40(1):A529–47.

42. Tong Y, Lombeyda S, Hirani AN, Desbrun M. Discrete Multiscale Vector Field Decomposition.

43. Freeman WJ, Rogers LJ, Holmes MD, Silbergeld DL. Spatial spectral analysis of human electrocorticograms including the alpha and gamma bands. J Neurosci Methods. 2000 Feb 15;95(2):111–21.

44. Mercier MR, Dubarry AS, Tadel F, Avanzini P, Axmacher N, Cellier D, et al. Advances in human intracranial electroencephalography research, guidelines and good practices. NeuroImage. 2022 Oct 15;260:119438.

45. Zhang Z, Moore JC. Chapter 6 - Empirical Orthogonal Functions. In: Zhang Z, Moore JC, editors. Mathematical and Physical Fundamentals of Climate Change [Internet]. Boston: Elsevier; 2015 [cited 2024 Apr 4]. p. 161–97. Available from: https://www.sciencedirect.com/science/article/pii/B9780128000663000061

46. Shinn M. Phantom oscillations in principal component analysis. Proc Natl Acad Sci [Internet]. 2023 Nov 28 [cited 2025 July 13];120(48). Available from: https://pnas.org/doi/10.1073/pnas.2311420120

47. Margulies DS, Falkiewicz M, Huntenburg JM. A cortical surface-based geodesic distance package for Python. GigaScience. 2016 Nov 1;5(suppl_1):s13742-016-0147-0-q.

48. Llinás R, Ribary U. Coherent 40-Hz oscillation characterizes dream state in humans. Proc Natl Acad Sci U S A. 1993 Mar 1;90(5):2078–81.

49. Massimini M, Huber R, Ferrarelli F, Hill S, Tononi G. The Sleep Slow Oscillation as a Traveling Wave. J Neurosci. 2004 Aug 4;24(31):6862–70.

50. Arieli A, Sterkin A, Grinvald A, Aertsen A. Dynamics of ongoing activity: explanation of the large variability in evoked cortical responses. Science. 1996 Sept 27;273(5283):1868–71.

51. London M, Roth A, Beeren L, Häusser M, Latham PE. Sensitivity to perturbations in vivo implies high noise and suggests rate coding in cortex. Nature. 2010 July;466(7302):123–7.

52. Freeman WJ. Mechanism and significance of global coherence in scalp EEG. Curr Opin Neurobiol. 2015 Apr;31:199–205.

53. Zanos TP, Mineault PJ, Pack CC. Removal of Spurious Correlations Between Spikes and Local Field Potentials. J Neurophysiol. 2011 Jan;105(1):474–86.

54. Kajikawa Y, Schroeder CE. How Local Is the Local Field Potential? Neuron. 2011 Dec 8;72(5):847–58.

55. Nauhaus I, Busse L, Carandini M, Ringach DL. Stimulus contrast modulates functional connectivity in visual cortex. Nat Neurosci. 2009 Jan;12(1):70–6.

56. Womelsdorf T, Schoffelen JM, Oostenveld R, Singer W, Desimone R, Engel AK, et al. Modulation of Neuronal Interactions Through Neuronal Synchronization. Science. 2007 June 15;316(5831):1609–12.

57. Besserve M, Lowe SC, Logothetis NK, Schölkopf B, Panzeri S. Shifts of Gamma Phase across Primary Visual Cortical Sites Reflect Dynamic Stimulus-Modulated Information Transfer. Kohn A, editor. PLOS Biol. 2015 Sept 22;13(9):e1002257.

58. Blakely T, Ojemann JG, Rao RPN. Short-time windowed covariance: A metric for identifying non-stationary, event-related covariant cortical sites. J Neurosci Methods. 2014 Jan;222:24–33.

59. Casimo K, Darvas F, Wander J, Ko A, Grabowski TJ, Novotny E, et al. Regional Patterns of Cortical Phase Synchrony in the Resting State. Brain Connect. 2016 July;6(6):470–81.

60. Arnulfo G, Wang SH, Myrov V, Toselli B, Hirvonen J, Fato MM, et al. Long-range phase synchronization of high-frequency oscillations in human cortex. Nat Commun [Internet]. 2020 Oct 23 [cited 2025 July 13];11(1). Available from: https://www.nature.com/articles/s41467-020-18975-8

61. Sauseng P, Klimesch W, Gruber W, Doppelmayr M, Stadler W, Schabus M. The interplay between theta and alpha oscillations in the human electroencephalogram reflects the transfer of information between memory systems. Neurosci Lett. 2002 May 17;324(2):121–4.

62. Takahashi K, Kim S, Coleman TP, Brown KA, Suminski AJ, Best MD, et al. Large-scale spatiotemporal spike patterning consistent with wave propagation in motor cortex. Nat Commun. 2015 May 21;6:7169.

63. Fröhlich F, McCormick DA. Endogenous electric fields may guide neocortical network activity. Neuron. 2010 July 15;67(1):129–43.

64. Anastassiou CA, Perin R, Markram H, Koch C. Ephaptic coupling of cortical neurons. Nat Neurosci. 2011 Feb;14(2):217–23.

65. Nicoll RA. A Brief History of Long-Term Potentiation. Neuron. 2017 Jan 18;93(2):281–90.

66. Ermentrout GB, Kleinfeld D. Traveling Electrical Waves in Cortex: Insights from Phase Dynamics and Speculation on a Computational Role. Neuron. 2001 Jan 1;29(1):33–44.

67. Mohan UR, Zhang H, Ermentrout B, Jacobs J. The direction of theta and alpha travelling waves modulates human memory processing. Nat Hum Behav. 2024 Mar 8;1–12.

68. Hindriks R. A methodological framework for inverse-modeling of propagating cortical activity using MEG/EEG. NeuroImage. 2020 Dec;223:117345.

69. Grabot L, Merholz G, Winawer J, Heeger DJ, Dugué L. Traveling waves in the human visual cortex: An MEG-EEG model-based approach. PLOS Comput Biol. 2025 Apr 17;21(4):e1013007.

70. Kupers ER, Edadan A, Benson NC, Zuiderbaan W, de Jong MC, Dumoulin SO, et al. A population receptive field model of the magnetoencephalography response. NeuroImage. 2021 Dec 1;244:118554.

71. Kupers ER, Benson NC, Winawer J. A visual encoding model links magnetoencephalography signals to neural synchrony in human cortex. NeuroImage. 2021 Dec 15;245:118655.

72. Piastra MC, Oostenveld R, Homölle S, Han B, Chen Q, Oostendorp T. How to assess the accuracy of volume conduction models? A validation study with stereotactic EEG data. Front Hum Neurosci [Internet]. 2024 Feb 12 [cited 2025 Aug 19];18. Available from: https://www.frontiersin.org/journals/human-neuroscience/articles/10.3389/fnhum.2024.1279183/full

73. Chaumon M, Puce A, George N. Statistical power: Implications for planning MEG studies. NeuroImage. 2021 June;233:117894.

74. King JR, Wyart V. The Human Brain Encodes a Chronicle of Visual Events at Each Instant of Time Through the Multiplexing of Traveling Waves. J Neurosci Off J Soc Neurosci. 2021 Aug 25;41(34):7224–33.

75. Alexander DM, Hermens DF, Keage HAD, Clark CR, Williams LM, Kohn MR, et al. Event-related wave activity in the EEG provides new marker of ADHD. Clin Neurophysiol Off J Int Fed Clin Neurophysiol. 2008 Jan;119(1):163–79.

76. Alexander DM, Flynn GJ, Wong W, Whitford TJ, Harris AWF, Galletly CA, et al. Spatio-temporal EEG waves in first episode schizophrenia. Clin Neurophysiol Off J Int Fed Clin Neurophysiol. 2009 Sept;120(9):1667–82.

77. Huntenburg JM, Bazin PL, Margulies DS. Large-Scale Gradients in Human Cortical Organization. Trends Cogn Sci. 2018 Jan;22(1):21–31.

78. Margulies DS, Ghosh SS, Goulas A, Falkiewicz M, Huntenburg JM, Langs G, et al. Situating the default-mode network along a principal gradient of macroscale cortical organization. Proc Natl Acad Sci. 2016 Nov;113(44):12574–9.

79. Alexander DM, Trengove C, van Leeuwen C. Donders is dead: cortical traveling waves and the limits of mental chronometry in cognitive neuroscience. Cogn Process. 2015 Nov;16(4):365–75.

80. Ezzyat Y, Kragel JE, Burke JF, Levy DF, Lyalenko A, Wanda P, et al. Direct Brain Stimulation Modulates Encoding States and Memory Performance in Humans. Curr Biol. 2017 May 8;27(9):1251–8.

81. Muller L, Miná č J, Nguyen TT. Algebraic approach to the Kuramoto model. Phys Rev E. 2021 Aug 5;104(2):L022201.

82. Fisher NI. Statistical Analysis of Circular Data [Internet]. Cambridge: Cambridge University Press; 1993 [cited 2024 Apr 7]. Available from: https://www.cambridge.org/core/books/statistical-analysis-of-circular-data/324A46F3941A5CD641ED0B0910B2C33F

83. Spagnolini U. 2-D phase unwrapping and instantaneous frequency estimation. IEEE Trans Geosci Remote Sens. 1995 May;33(3):579–89.

84. Herrmann CS, Grigutsch M, Busch NA. EEG oscillations and wavelet analysis. In: Event-related potentials: A methods handbook [Internet]. MIT Press; 2005 [cited 2024 May 20]. p. 229–59. Available from: https://hdl.handle.net/11858/00-001M-0000-002B-F616-F

85. Huang NE, Shen Z, Long SR, Wu MC, Shih HH, Zheng Q, et al. The empirical mode decomposition and the Hilbert spectrum for nonlinear and non-stationary time series analysis. Proc R Soc Lond Ser Math Phys Eng Sci. 1998 Mar 8;454(1971):903–95.

86. Cohen MX. Analyzing Neural Time Series Data: Theory and Practice [Internet]. The MIT Press; 2014 [cited 2025 July 13]. Available from: https://direct.mit.edu/books/monograph/4013/Analyzing-Neural-Time-Series-DataTheory-and

87. Alamia A, VanRullen R. Alpha oscillations and traveling waves: Signatures of predictive coding? Kohn A, editor. PLOS Biol. 2019 Oct 3;17(10):e3000487.

88. Gaspar FJ, Gracia JL, Lisbona FJ. Fourier Analysis for Multigrid Methods on Triangular Grids. SIAM J Sci Comput. 2009 Jan;31(3):2081–102.

89. Sivakumar SS, Namath AG, Galán RF. Spherical Harmonics Reveal Standing EEG Waves and Long-Range Neural Synchronization during Non-REM Sleep. Front Comput Neurosci [Internet]. 2016 June 22 [cited 2025 July 13];10. Available from: http://journal.frontiersin.org/Article/10.3389/fncom.2016.00059/abstract

90. Cabral J, Fernandes FF, Shemesh N. Intrinsic macroscale oscillatory modes driving long range functional connectivity in female rat brains detected by ultrafast fMRI. Nat Commun [Internet]. 2023 Feb 6 [cited 2025 July 13];14(1). Available from: https://www.nature.com/articles/s41467-023-36025-x

91. Daini D, Ceccarelli G, Cataldo E, Jirsa V. Spherical-harmonics mode decomposition of neural field equations. Phys Rev E [Internet]. 2020 Jan 6 [cited 2025 July 13];101(1). Available from: https://link.aps.org/doi/10.1103/PhysRevE.101.012202

92. MacDowell CJ, Buschman TJ. Low-Dimensional Spatio-Temporal Dynamics Underlie Cortex-Wide Neural Activity.

93. Robinson PA, Zhao X, Aquino KM, Griffiths JD, Sarkar S, Mehta-Pandejee G. Eigenmodes of brain activity: Neural field theory predictions and comparison with experiment. NeuroImage. 2016 Nov;142:79–98.

94. Rosso M, Fernández-Rubio G, Keller PE, Brattico E, Vuust P, Kringelbach ML, et al. FREQ-NESS Reveals the Dynamic Reconfiguration of Frequency-Resolved Brain Networks During Auditory Stimulation. Adv Sci. 2025;12(20):2413195.

95. Cline AK, Dhillon IS. Computation of the Singular Value Decomposition. In: Handbook of Linear Algebra. Chapman and Hall/CRC; 2006.

96. Brunton SL, Kutz JN. Cambridge Aspire website. Cambridge University Press; 2022 [cited 2025 Aug 20]. Data-Driven Science and Engineering: Machine Learning, Dynamical Systems, and Control. Available from: https://www.cambridge.org/highereducation/books/data-driven-science-and-engineering/6F9A730B7A9A9F43F68CF21A24BEC339

97. Kajikawa Y, Schroeder CE. How Local Is the Local Field Potential? Neuron. 2011 Dec 8;72(5):847–58.

98. Shinn M. Phantom oscillations in principal component analysis. Proc Natl Acad Sci U S A. 2023 Nov 28;120(48):e2311420120.

99. Fourier JBJ. Théorie Analytique de la Chaleur. Paris: Didot; 1822.

100. Bullock TH, McClune MC, Achimowicz JZ, Iragui-Madoz VJ, Duckrow RB, Spencer SS. EEG coherence has structure in the millimeter domain: subdural and hippocampal recordings from epileptic patients. Electroencephalogr Clin Neurophysiol. 1995 Sept;95(3):161–77.

101. Zvyagintsev M, Nikolaev AR, Mathiak KA, Menning H, Hertrich I, Mathiak K. Predictability modulates motor–auditory interactions in self-triggered audio–visual apparent motion. Exp Brain Res. 2008 Aug 1;189(3):289–300.

102. Sheridan P, Hintz T, Alexander D. Pseudo-invariant image transformations on a hexagonal lattice. Image Vis Comput. 2000 Aug;18(11):907–17.

Supplementary Figures

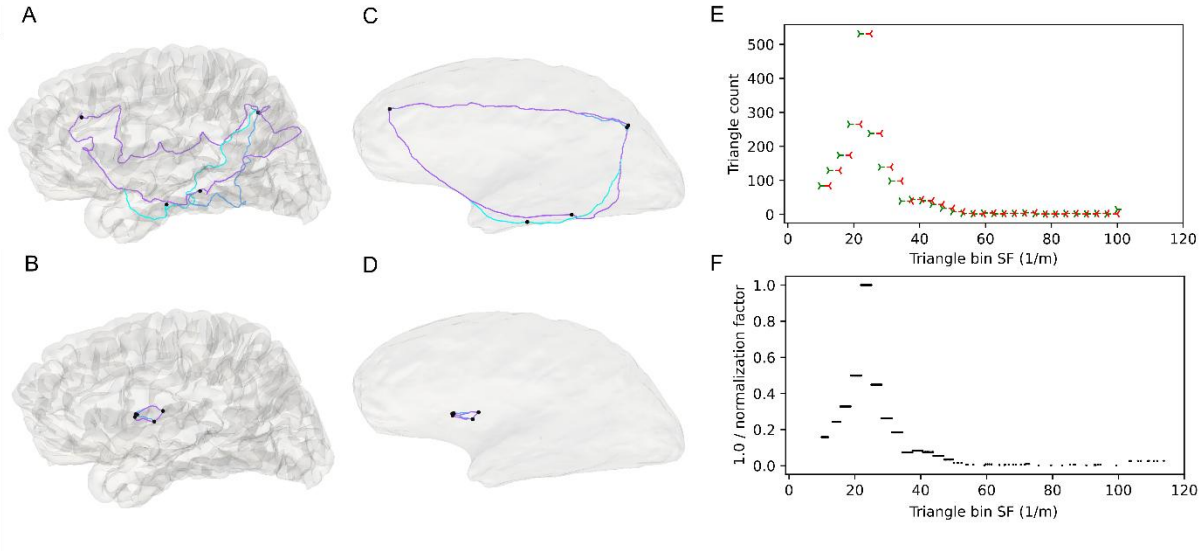

Supplementary Figure 1. *Examples of the equilateral triangles between contacts used in the multi-scale differencing.* ***A****. Cortical surface for one participant, with contacts (black dots) and geodesic distances (coloured lines) corresponding to edges of triangles in the largest triangle bin used in the multi-scale differencing.* ***B****. Contacts and geodesic distances corresponding to the smallest triangle bin for this participant.* ***C*** *&* ***D****. Same data as* ***A*** *&* ***B*** *but shown on the inflated cortex. While the geodesic distances are calculated on the folded cortex, the inflated cortex gives a clearer view of the equilateral triangles connected by shortest distances across the cortex.* ***E****. Distribution of triangle sizes (as equivalent SFs) for this participant. Left green wedge and right red wedge indicate the bounds of each triangle bin.* ***F****. Normalization factor applied to each triangle of contacts in the calculation of the SF spectrum. This effectively flattens the distribution to give equal weighting to triangles across the size range.*

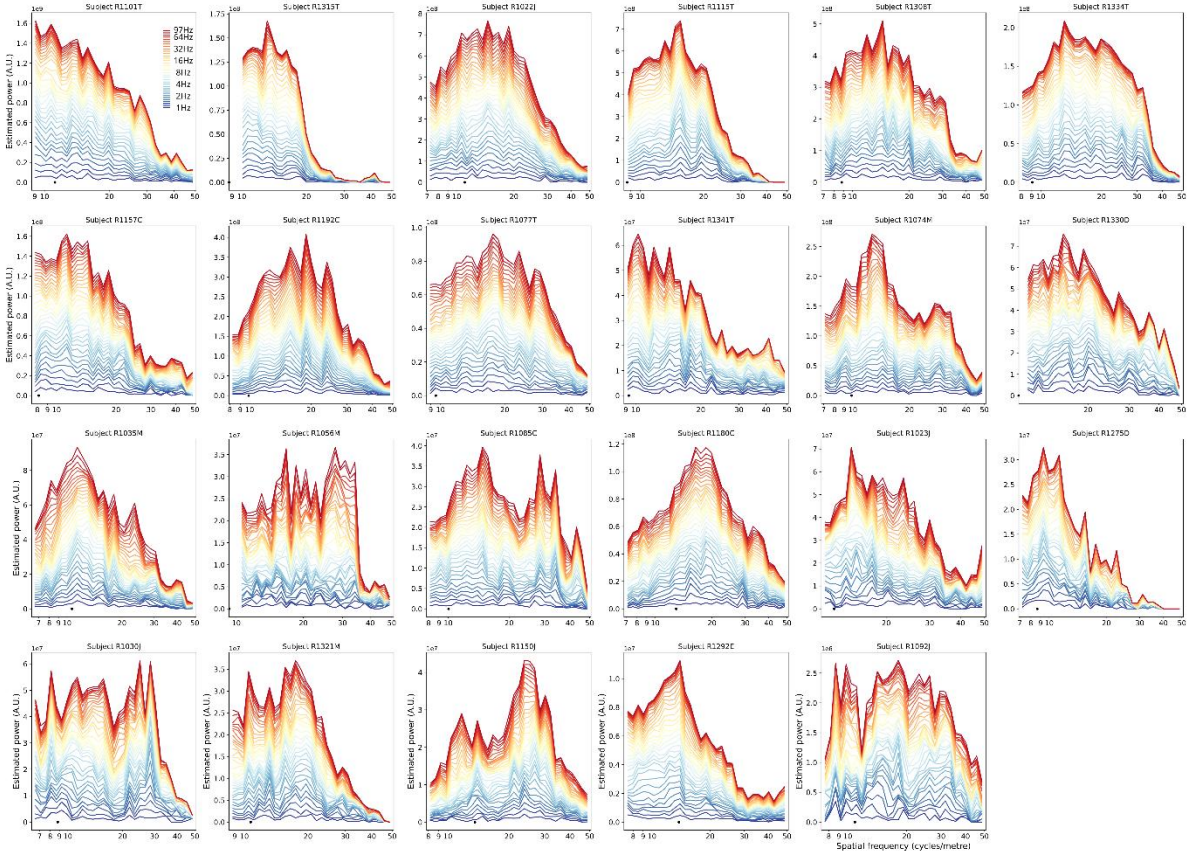

Supplementary Figure 2. *Stacked SF spectra, across temporal frequencies 1.0 to 97.0Hz (colour scale), for all participants. Participant's plots are ordered by number of equilateral triangles, highest (n=11051) to lowest (n=66). The largest triangle size for each participant is indicated with the black dot.*

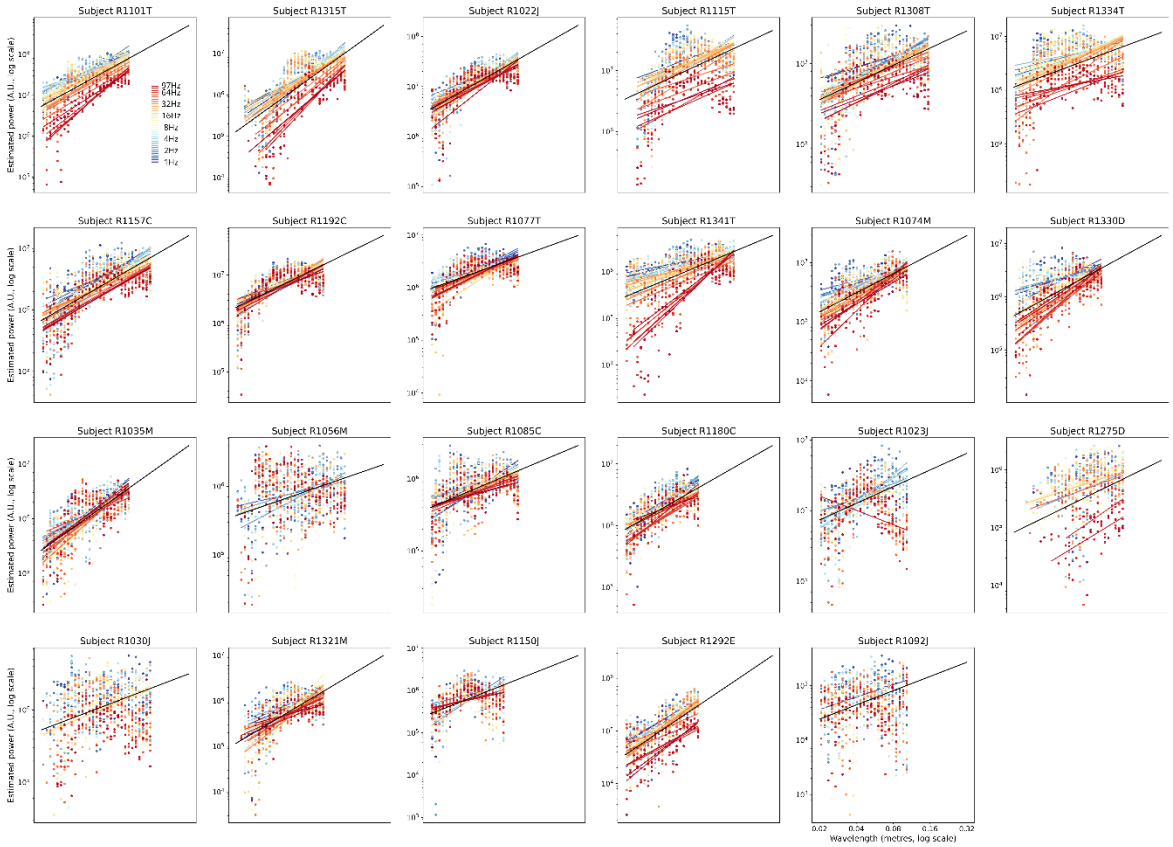

Supplementary Figure 3. *Regression lines for wavelength versus SF power at temporal frequencies 1.0 to 97.0Hz (coloured lines), for all participants. Participant's plots are ordered by number of triangles, from highest (n=11051) to lowest (n=66). Regressions are from the values of the spectra shown in* ***Supplementary Figure 2*** *(only individual regression lines significant at p<0.05 shown). Spectrum values are shown with coloured dots. The mean regression line for each participant (mean of slopes and offsets of significant regressions) is shown with a black line and extended to 0.32m wavelength for visualization purposes.*

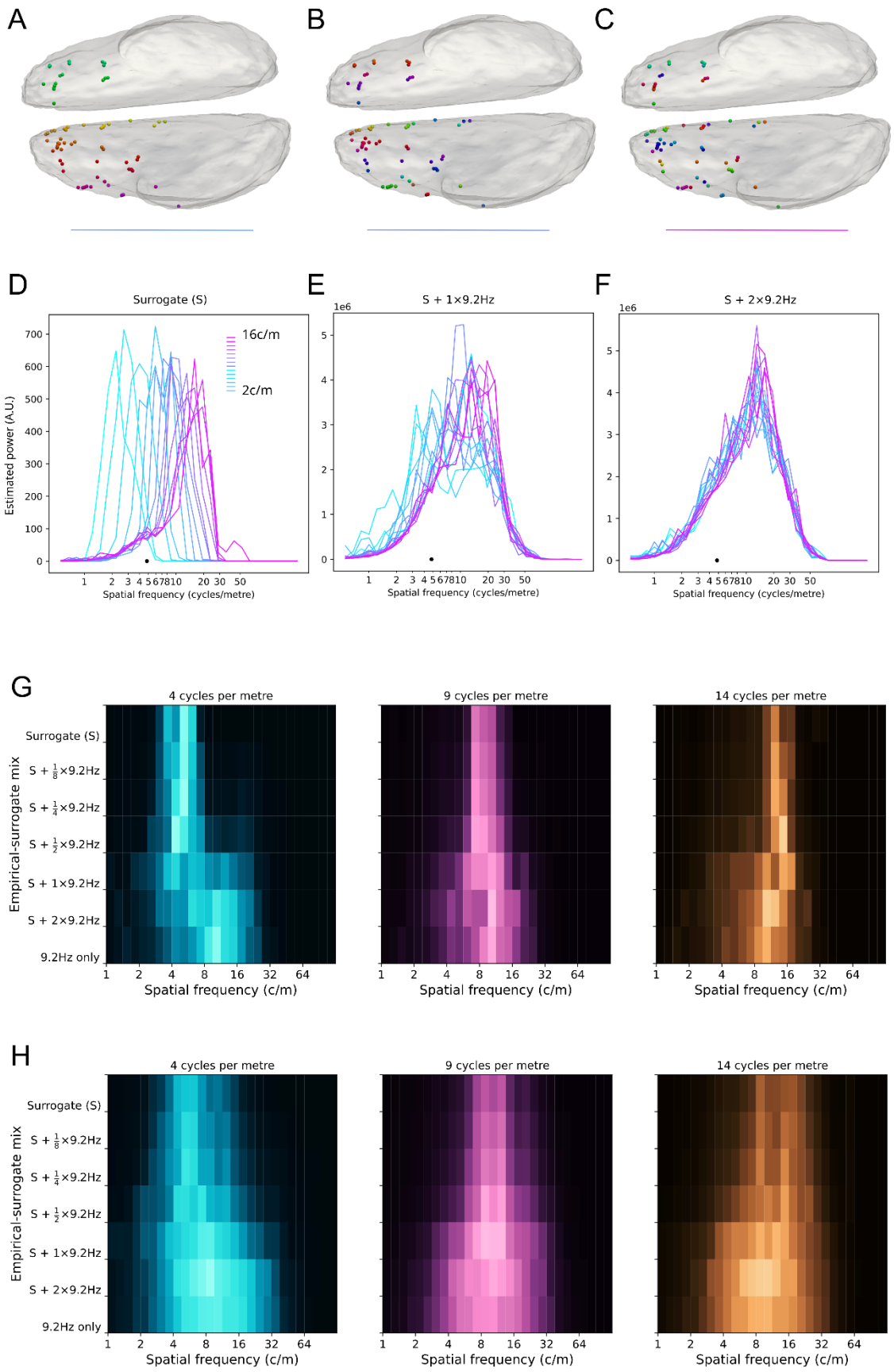

Supplementary Figure 4. *More surrogate testing examples.* ***A****. Participant's inflated cortex with surrogate phase values, here in the form of a left-right gradient at 4c/m. Grey-matter*

*contacts are shown as spheres, with phase shown on the colour scale. Coloured lines below each cortex refer to the colour spectra in **D**, **E** & **F**.**B**. Same conventions as **A**, except 9c/m. **C**. Same conventions as **A**, except 14c/m. **D**. Spectra for pure surrogate signals injected as a left-right gradient to the participant in **A**, over a range of SFs 2 to 16 c/m. Black dot shows maximum array distance for this participant. **E**. Same as **D**, except for evenly weighted surrogate and empirical signals. **F**. Same as **E**, except for 1:2 surrogate to empirical signal. **G**. Effects of injection of veridical SF surrogate signal on the spectrum derived from the empirical signal. Left panel shows the spectrum of a pure surrogate signal (S) with the left-right gradient and a SF at 4c/m (top row, same surrogate signal as shown in **A**). The empirical spectrum for phase of this participant at a centre frequency of 9.2Hz is also shown (bottom row). The effects of different weightings of empirical and surrogate signal vary vertically over the plot. Middle panel follows the same conventions, except a surrogate signal at 9c/m is shown (same surrogate signal as shown in **B**). Right panel shows the effect of a surrogate signal at 14c/m (shown in **C**). **H**. Participant averaged spectra (n=23), conventions otherwise the same as **G**.*

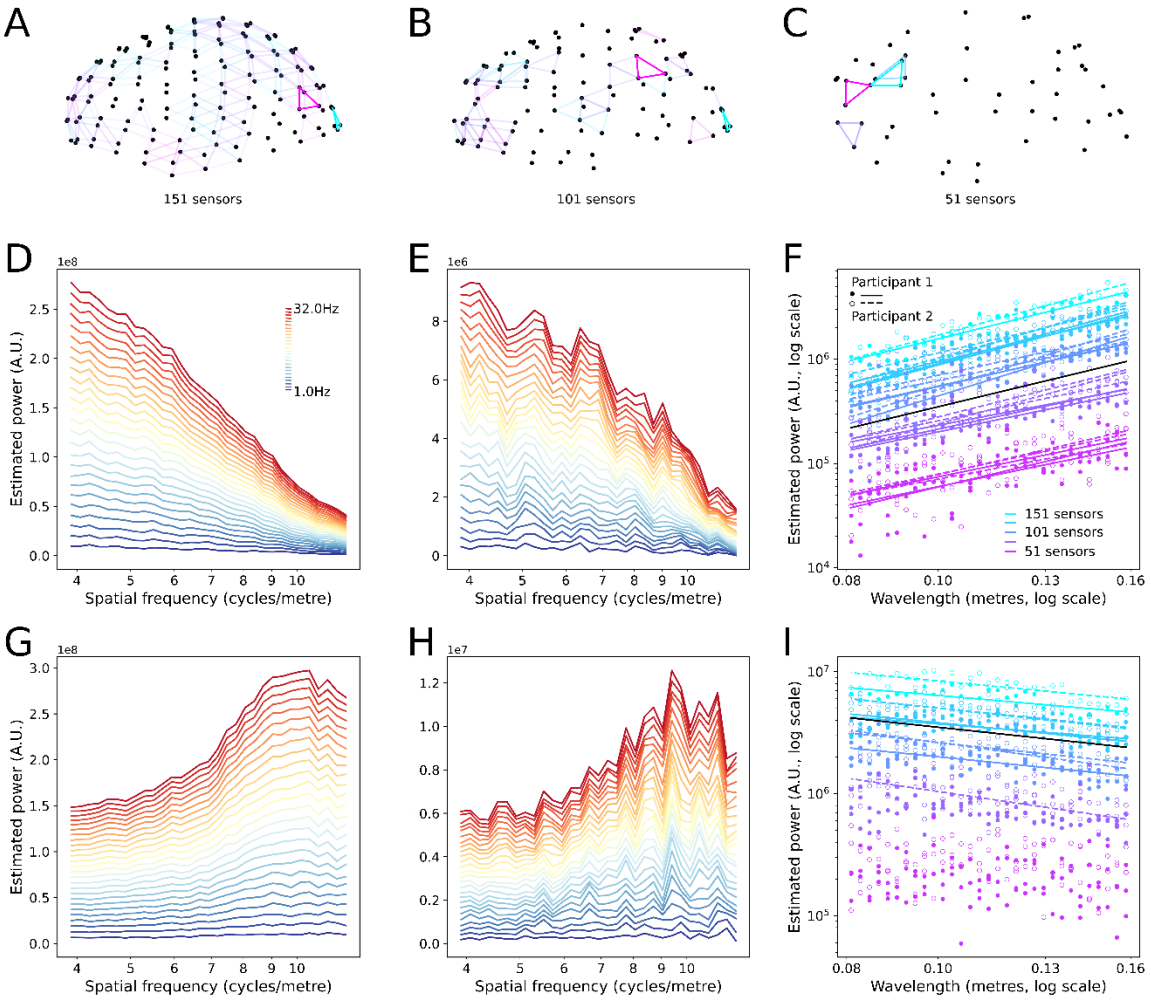

Supplementary Figure 5. *Effects of randomly removing sensors from a semi-regular array.* ***A****. MEG sensor array, with 151 sensors, showing triangles of sensors in the size bin with mean size 0.21m (smallest and largest triangle in this bin without transparency).* ***B****. MEG sensor array, with one third of sensors removed, conventions same as* ***A****.* ***C****. MEG sensor array, with two thirds of sensors removed, conventions same as* ***A****.* ***D****. Stacked spatial frequency spectrum of a single participant for temporal frequencies 1.0 (blue) to 32.0Hz (red), estimated from the sensory array (and corresponding time-series) shown in* ***A****.* ***E****. Stacked spatial frequency spectrum of a single participant for temporal frequencies 1.0 (blue) to 32.0Hz (red), estimated from the sensory array (and corresponding time-series) shown in* ***C****.* ***F****. Wavelength by spatial frequency power regression lines for two MEG participants at 9.2Hz, shown with closed and open circles. Light blue shows the regressions for full sensor arrays, violet shows the regression lines for the sensor arrays with two thirds of sensors removed. Contacts were removed pseudo-randomly in five steps between these ranges (inclusive), in three runs. Only regressions that were significant (p<0.001) are shown as lines. Mean slope over all regressions shown with black line (p<0.001, permutation testing).* ***G****. Stacked spatial frequency spectrum from the surrogate MEG data with reversed spatial frequency spectrum, conventions same as* ***D*** *(all sensors).* ***H****. Stacked spatial frequency spectrum from the surrogate MEG data with reversed spatial frequency spectrum, conventions same as* ***E*** *(two thirds of sensors removed).* ***I****. Wavelength by spatial frequency power regression lines for two MEG participants with reversed spatial frequency spectrum at 9.2Hz, conventions same as* ***F****.*

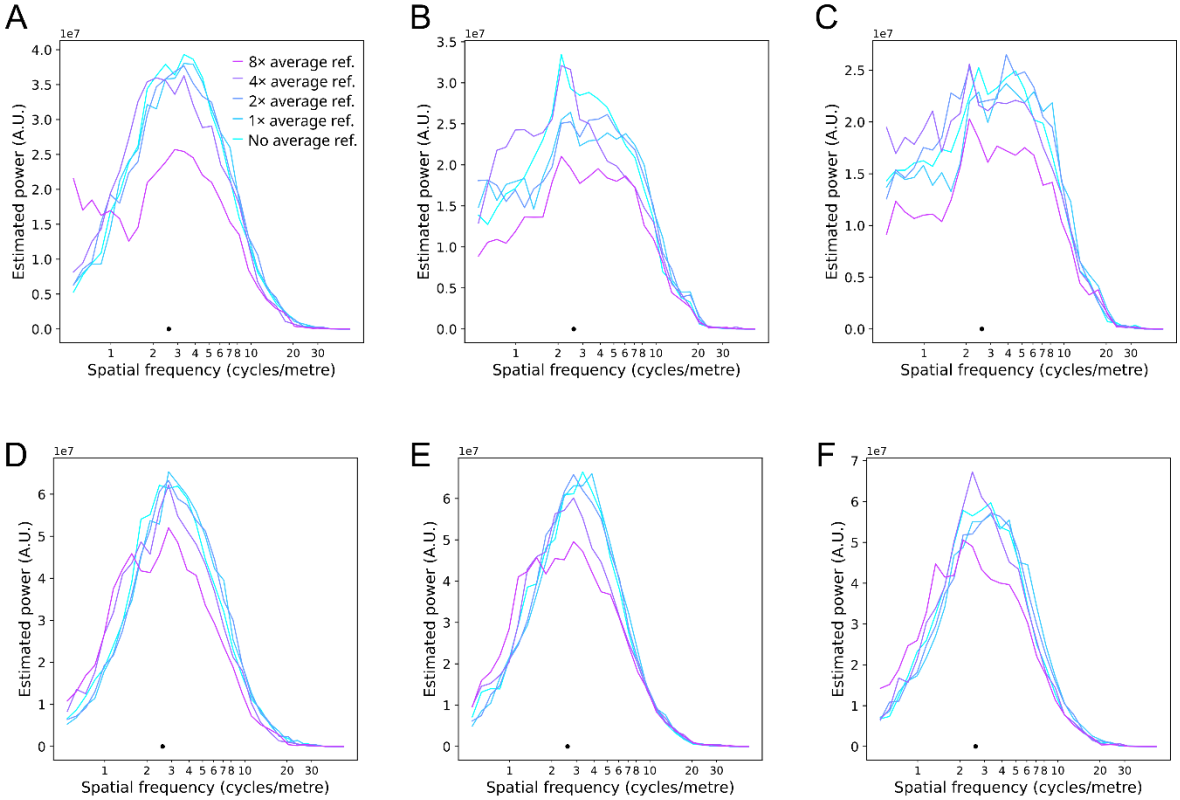

Supplementary Figure 6. *Surrogate testing for the effect of average reference and removal of DC component on the phase spatial spectrum.* ***A****. Spatial frequency spectrum of phase for a single MEG participant, at 1Hz with increasing average reference (colour scale). DC component has not been removed. Black dot shows the spatial frequency corresponding to the maximum inter-sensor distance.* ***B****. Same conventions as A, except 9.2Hz.* ***C****. Same conventions as A, except 32.0Hz.* ***D****. Spatial frequency spectrum of phase at 1Hz with increasing average reference. DC component has been removed.* ***E****. Same as* ***D****, except 9.2Hz.* ***F****. Same as* ***D****, except 32.0Hz.*

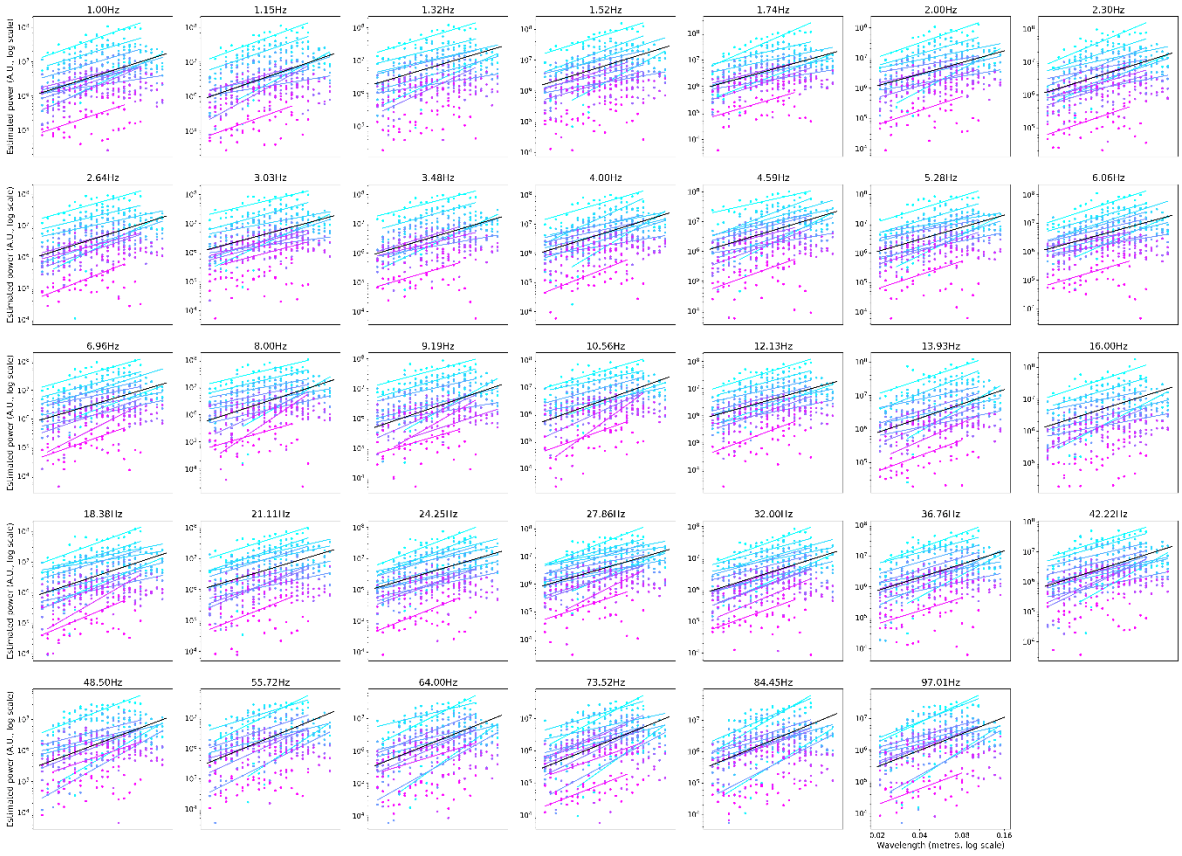

Supplementary Figure 7. *Cross-participant analyses by temporal frequency. Regression lines for (logarithm of) wavelength versus SF power at each centre TF, for all participants. In each plot, participants are ordered from most number of triangles (n=11051; light blue) to least number of triangles (n=56; lilac). Spectra values are shown as coloured dots (data from* ***Supplementary Figure 2****). Only individual participant (at a given frequency) regressions that were significant at p<0.05 are shown as regression lines in each plot. The mean slope and offset for all significant regressions at the relevant temporal frequency are shown as a black line.*

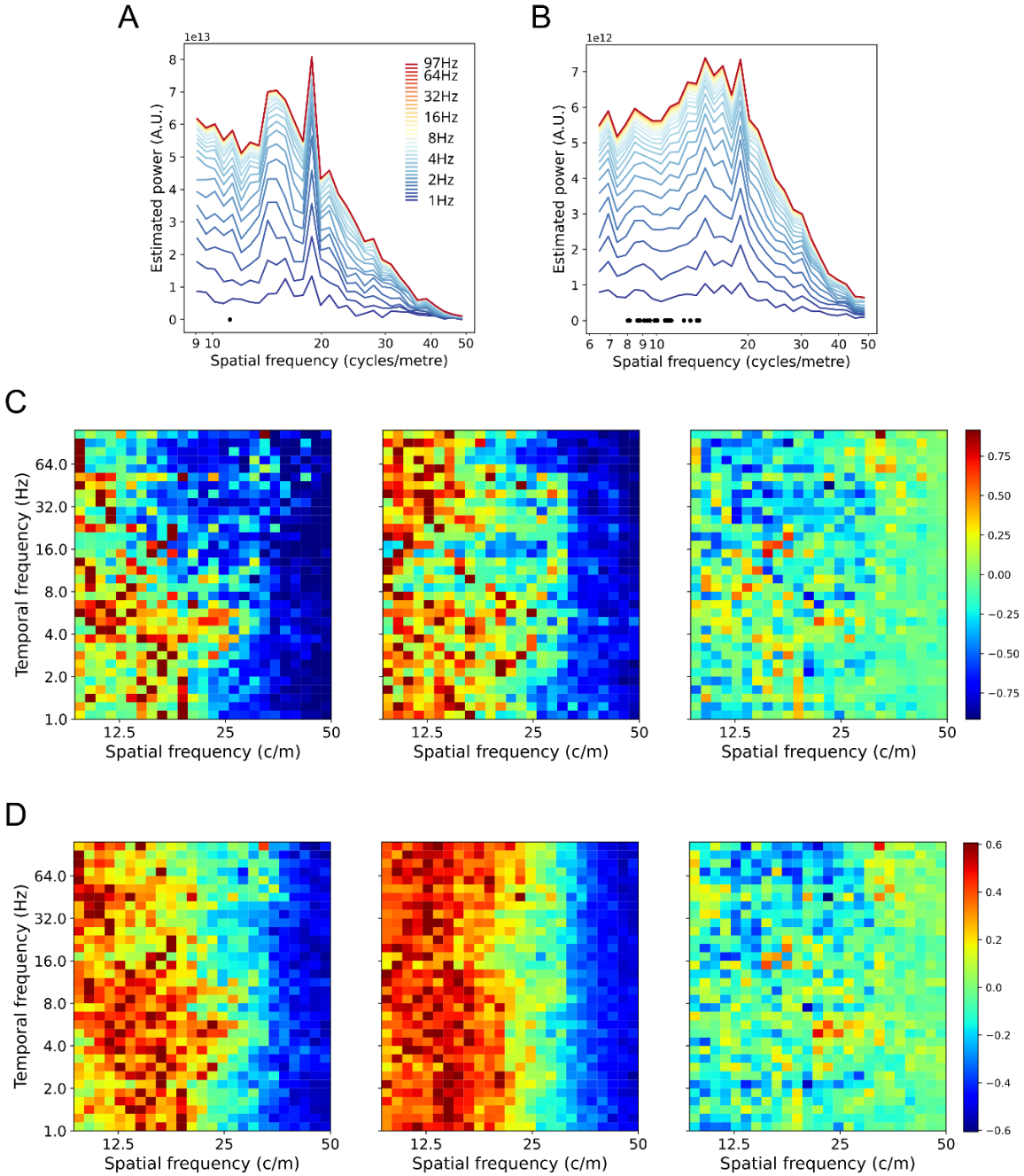

Supplementary Figure 8. *Effects of including TF power on SF spectra.* ***A****. Participant's stacked SF spectra with TF power included in the estimate. TFs are shown on the colour scale. Compare with the same participant, phase only spectra, Figure 5H. Higher TFs have smaller contributions to SF power due to the smaller amplitudes of higher TF signal.* ***B****. Aggregate stacked SF spectra with TF power included, over 23 participants. Compare with the aggregate stacked spectra shown in* ***Figure 7C****.* ***C****. Participant's SF spectra as SF by TF plot. Power values are shown as colours. In order to visualize the SFs at higher TFs, the SF power has been normalized between 0 (cold) and 1 (hot) at each temporal frequency, prior to plotting. The left plot shows the SF spectra with TF power included (data taken from* ***A****). The middle plot shows the phase only SF spectra (data taken from* ***Figure 5H****). The right plot shows the difference between the two SF spectra, with differences given on the colour scale.*
D*. Aggregate spectra for 23 participants, conventions the same as* ***C****. Data are taken from* ***B*** *and* ***Figure 7C*** *for the left and middle plots.*

A

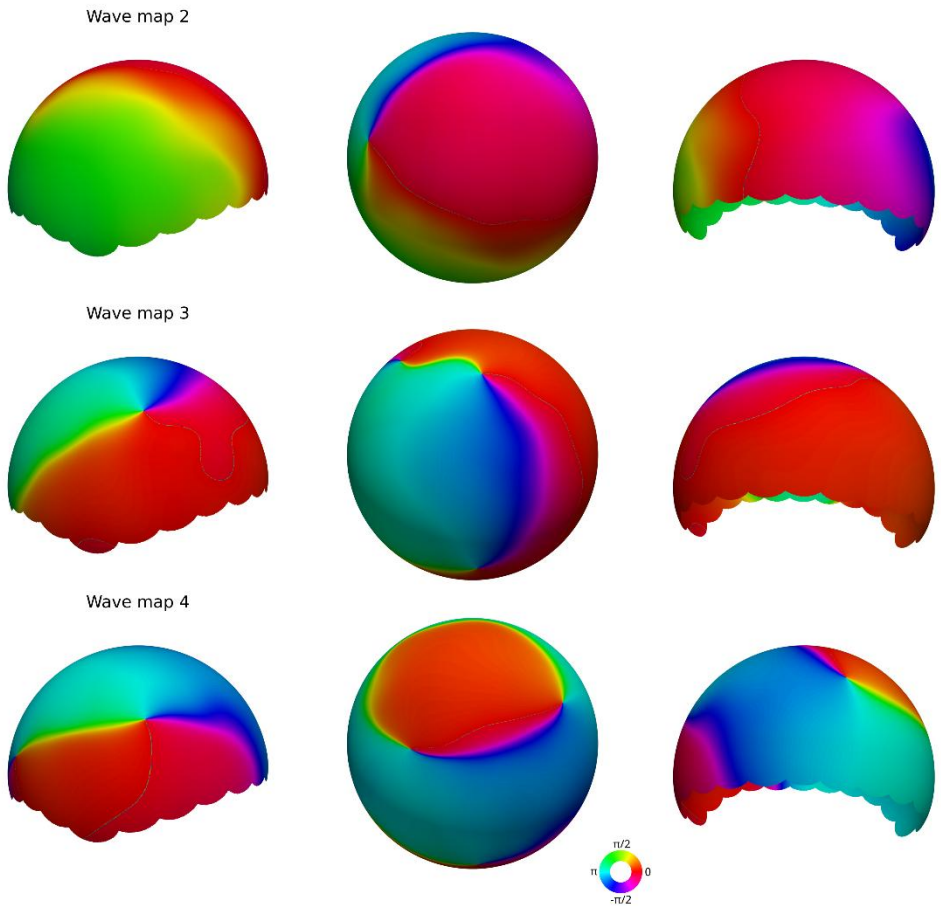
Wave map 2
Wave map 3
Wave map 4
π/2
π
0
-π/2

B

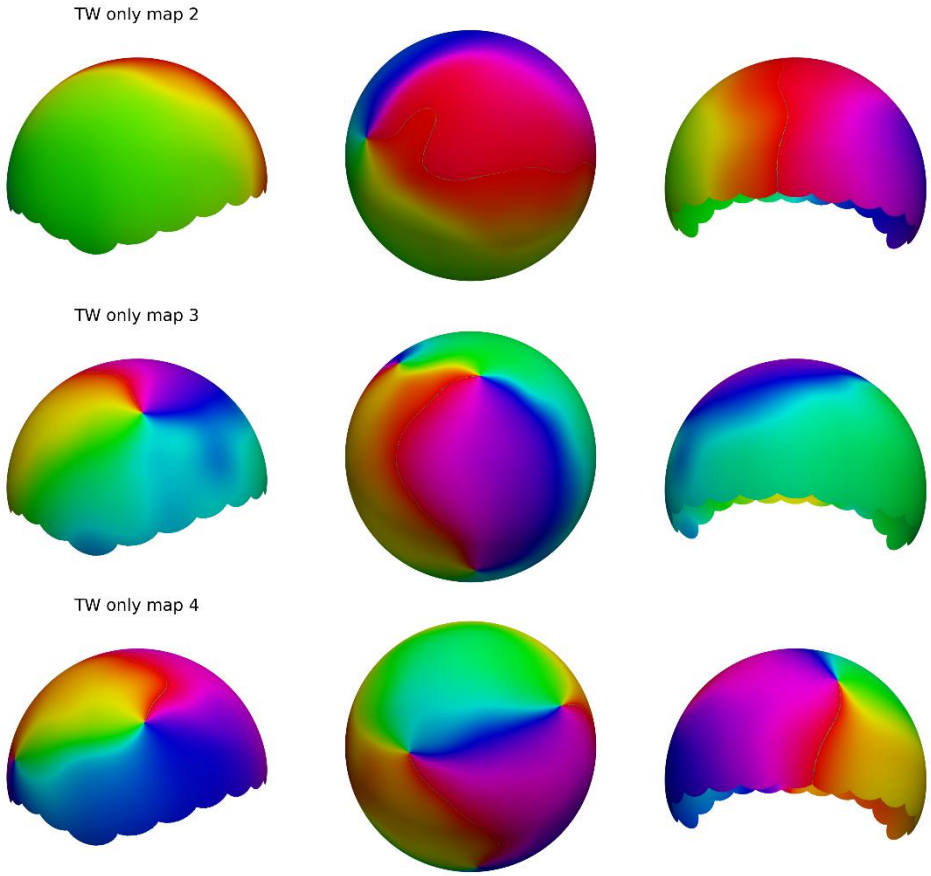
TW only map 2
TW only map 3
TW only map 4

Supplementary Figure 9*. Illustration of the removal of negative SF components.* ***A****. Three LSVs from an MEG subject at 6.0Hz. These LSVs showed stronger than usual standing wave patterns in components 3 and 4. The standing wave patterns can arise from SVD, even when the underlying samples are all pure TWs, if the balance of the two directions is almost equal. As discussed in Alexander et al. (2016), standing wave patterns give rise to misleading estimates of phase velocity (here, to SF), since the interference pattern of the two wave directions creates both slowly changing gradients (at the peaks and troughs of the standing wave) and fast changing gradients (at the inflection points of the standing wave). Panels show left, top and back views of MEG array, with phase values (colour scale) interpolated for visualization purposes.* ***B****. Same data as* ***A****, except the negative SF components have been removed, leaving only the positive SFs. The gradients of phase are smoother, reflecting the SF of the underlying Fourier-like component of the phase. Conventions the same as A.*

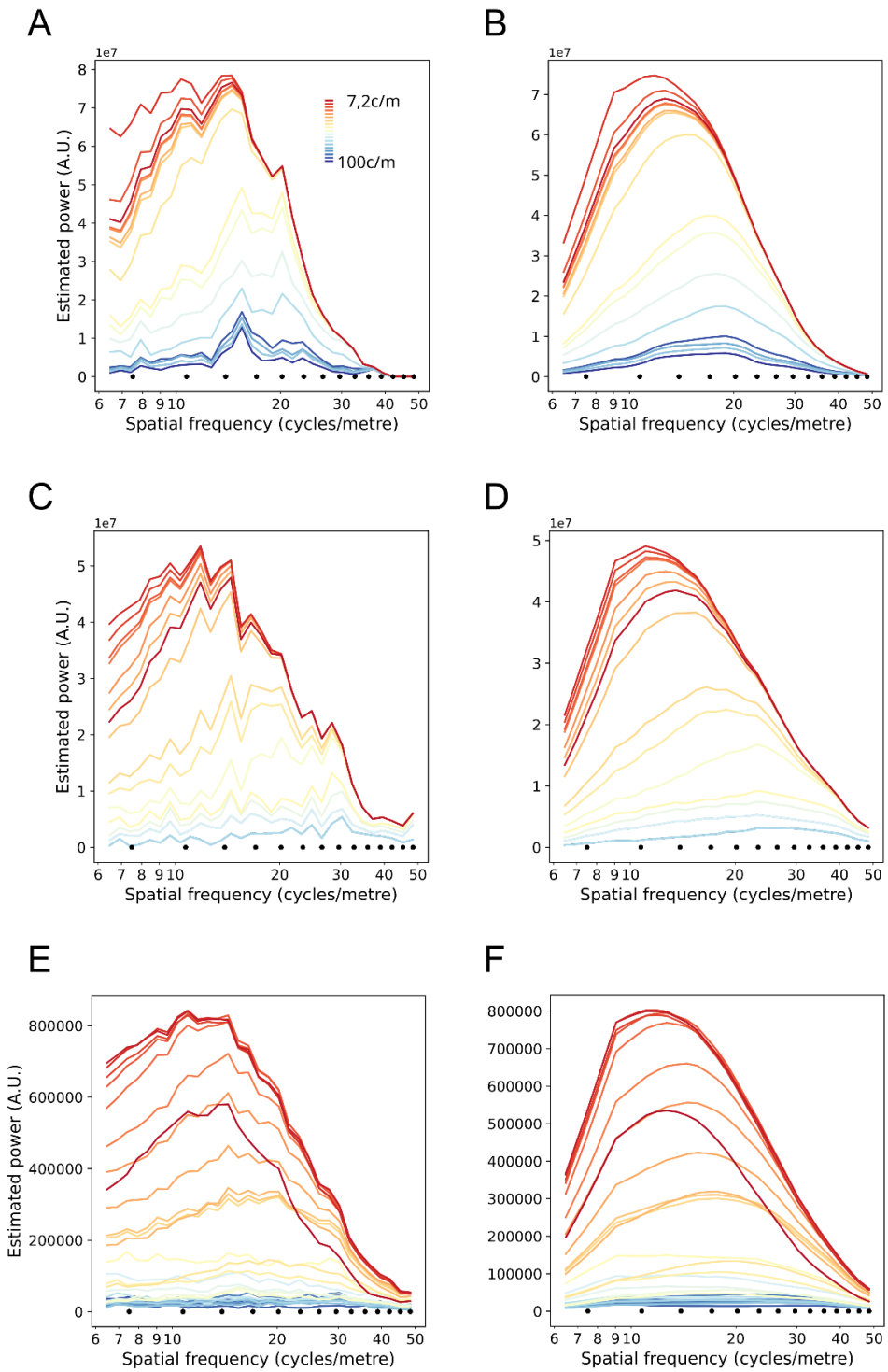

***Supplementary Figure 10**. Effects of bin size and calculation of spectral peak. **A**. Spectra for an individual participant, aggregated by triangle bin size. Triangle bin sizes are indicated with black dots (as 1/m, shown out to 50c/m only) and associated spectra are shown with coloured lines. **B**. Same data as **A**, except spectra have been smoothed with a rolling average over 10 steps. Peaks of spectra are read off from the maxima of these curves. **C**. Spectra for another individual participant, conventions same as **A**. **D**. Smoothed spectra for participant shown in **C**. **E**. Mean spectra across 23 participants, aggregate by triangle bin size. **F**. Smoothed spectra for **E**.*

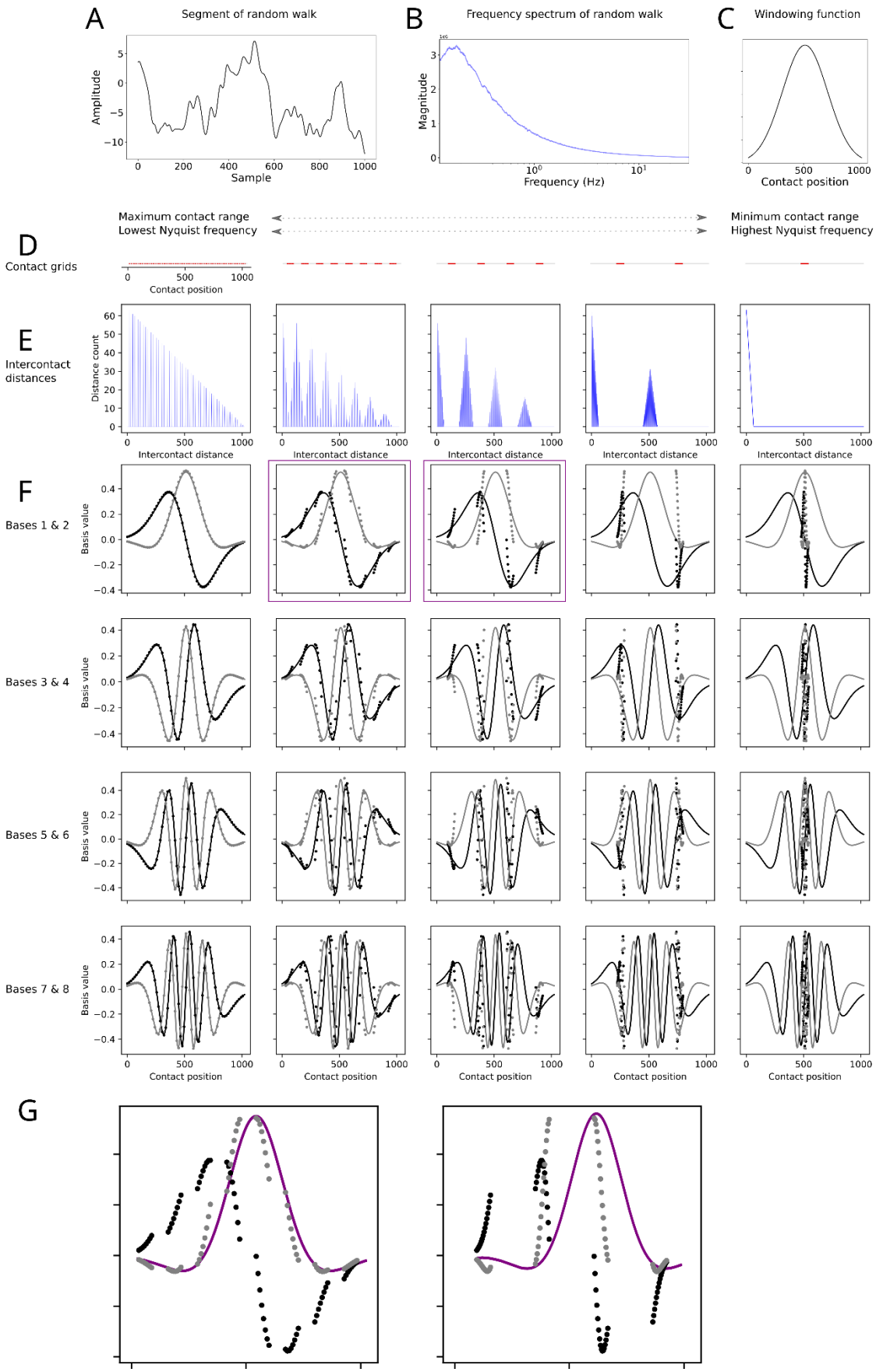

Supplementary Figure 11. *Surrogate analysis of multi-scale contact arrays using random walk data.* ***A***. *A random walk (t = 1,000,000) is constructed by taking cosine of a randomly*

generated number between -π and π and adding it to the cumulative total. The series is high-pass filtered to remove the DC offset, trend and large scale fluctuations. ***B****. The frequency spectrum of the filtered random walk, generated using FTT. Since the data are one-dimensional they can be regarded as temporal (frequencies in Hz) or as sampled in one spatial dimension (frequencies in c/m).* ***C****. A Hankel matrix was constructed from successive segments of w = 1024 samples, windowed by a Gaussian function (shown). The Hankel matrix* $\mathbf{A}_{wT}$*, where T = t - w/2, is submitted to the SVD.* ***D****. Multi-scale contact grids (red dots) were constructed by applying modulo arithmetic to an initial sparse but regularly space grid (first panel). The next three grids (panels 2-4) are comprised of separated individual contacts, but the spatial scale of the Figure is not sufficient to reveal them as separated dots.* ***E****. Histograms of intercontact distances for the five contact arrays shown in* ***D****.* ***F****. LSVs from five SVD analyses using each of the measurement arrays to sample the same random walk. Successive pairs of components are shown down each column, showing an increase in SF tuning down the column. Each row shows a pair of components (e.g. 1st and 2nd components, with lowest SF, in the first row), as extracted from the five SVD analyses. The SF properties of the component is strongly a function of the characteristic intercontact distances in the multi-scale arrays. The LSVs from the original SVD (****Figure 3A****) are shown as grey and black lines for comparison purposes.* ***G****. High SF representations are visually apparent in each of the LSVs produced from multi-scale SVDs. Interpolation of a sinusoid from the leading contact in each local neighbourhood (purple line) also reveals that low SF components are represented in the LSVs. Plots are the same as* ***F****, row 1, panels 2 & 3 (indicated by purple squares).*

Supplementary Video 1. *Dorsal view of one participant's dominant spatial patterns of phase at 3.5Hz.*

The video shows the time-series of a low rank model of phase dynamics, constructed from the first three LSVs. Together, these LSVs account for 43.6% of the variance in phase. This low SF activity dominates the dynamics. The entire video comprises 6s of cortical activity. Colour values are cosine of the phase (yellow=-1, red=1). Values between contacts are interpolated for visualization purposes. Anterior region of cortex is to the left.

Supplementary Video 2. *Anterior view of one participant's dominant spatial patterns of phase at 8.0Hz.*
The video shows the time-series of a low rank model of phase dynamics, constructed from the first four LSVs. Together, these LSVs account for 39.3% of the variance in phase. This low SF activity dominates the dynamics. The entire video comprises 6s of cortical activity. Colour values are cosine of the phase (yellow=-1, red=1). Values between contacts are interpolated for visualization purposes. Left hemisphere of cortex is to the left.

Supplementary Video 3*. Left view of one participant's dominant spatial patterns of phase at 8.0Hz.*
The video shows the time-series of a low rank model of phase dynamics, constructed from the first three LSVs. Together, these LSVs account for 40.8% of the variance in phase. This low SF activity dominates the dynamics. The entire video comprises 6s of cortical activity. Colour values are cosine of the phase (yellow=-1, red=1). Values between contacts are interpolated for visualization purposes. Anterior region of cortex is to the left.